POLITECNICO DI TORINO
Repository ISTITUZIONALE

Novel discrete flexible multibody model for ball bearings with deformable rings in harmonic drive applications

Original
Novel discrete flexible multibody model for ball bearings with deformable rings in harmonic drive applications / Guida, R., De Martin, A.. - In: MECHANISM AND MACHINE THEORY. - ISSN 0094-114X. - 229:(2026). [10.1016/j.mechmachtheory.2026.106579]

Availability:
This version is available at: 11583/3015373 since: 2026-09-11T11:23:00Z

Publisher:
Elsevier

Published
DOI:10.1016/j.mechmachtheory.2026.106579

Terms of use:

This article is made available under terms and conditions as specified in the corresponding bibliographic description in the repository

Publisher copyright

(Article begins on next page)

26 November 2026

Mechanism and Machine Theory 229 (2026) 106579

Contents lists available at ScienceDirect

Mechanism and Machine Theory

journal homepage: www.elsevier.com/locate/mechmt

Research paper

Novel discrete flexible multibody model for ball bearings with deformable rings in harmonic drive applications

Roberto Guida *, Andrea De Martin

Politecnico di Torino, Deparment of Mechanical and Aerospace Engineering, Corso Duca degli Abruzzi, 24, Torino, 10129, Piemonte, Italy

ARTICLE INFO

Keywords:
Deformable bearings
Multibody modeling
Discrete flexible multibody
Harmonic reducer

ABSTRACT

Deformable ball bearings play a critical role in harmonic drives, where the transmission principle relies on elastic deformation of thin-walled components. Classical models based on rigid rings or computationally expensive FEM approaches struggle to capture the dynamic behaviour required for accurate description and/or have too expensive simulation costs. This work presents a discrete flexible multibody modelling approach in which the inner ring, rolling elements, and a discretized outer ring are represented as interacting bodies connected by spring-damper systems, nonlinear Hertzian contacts, and beam-based homogenization and anchoring forces. The outer ring deformation is reconstructed dynamically by modelling each circumferential sector as a simply supported Euler-Bernoulli beam, enabling a computationally efficient yet physically consistent description of ring curvature, sector coupling, and preload effects. Dynamic analyses show the emergence of consistent and predictable deformation-induced interactions. The proposed formulation, exploiting the discrete flexible multibody approach, bridges the gap between simplified analytical models and full FEM, providing an efficient tool suitable for integration into complete harmonic drive simulations and offering improved capabilities for dynamic performance prediction, and health-monitoring applications.

1. Introduction

Bearings are fundamental machine elements that constrain relative motion, carry loads, and reduce friction between moving parts [1,2] in robotics [3], aerospace [4], and industrial automation [5]. Depending on the operating conditions, different types are used, such as ball, roller, and specialized bearings. In most power-transmission and precision-mechanical systems analytical models, they are represented as nominally rigid rolling or sliding interfaces, whose principal design variables include load capacity, stiffness, friction, and service life [6]. However, in thin-ring bearings, like the ones in the harmonic drive systems [7], the assumption of rigidity is no longer valid: elastic deformation alters the internal geometry and load distribution [8].

A deformable bearing departs from the rigid-bearing ideal by allowing, and in some cases relying on, controlled elastic deformation of one or both bearing races or of the supporting structure. This deformability modifies the distribution of contact loads, introduces compliance and damping at the interfaces, and influences the system's dynamic response to external excitations and manufacturing or assembly errors. Explicitly modeling these elastic effects becomes essential when the bearing not only supports motion but also contributes actively to the mechanism's kinematics and compliance [9,10].

In fact accurately describing bearing deformability is important for several practical reasons. First, elastic deformation governs the load distribution along the contact region, directly affecting local stress, wear rate, and fatigue life [11], particularly critical

* Corresponding author.
E-mail address: roberto.guida@polito.it (R. Guida).

https://doi.org/10.1016/j.mechmachtheory.2026.106579
Received 22 January 2026; Received in revised form 23 July 2026; Accepted 17 August 2026
0094-114X/© 2026 The Authors. Published by Elsevier Ltd. This is an open access article under the CC BY-NC-ND license (http://creativecommons.org/licenses/by-nc-nd/4.0/).

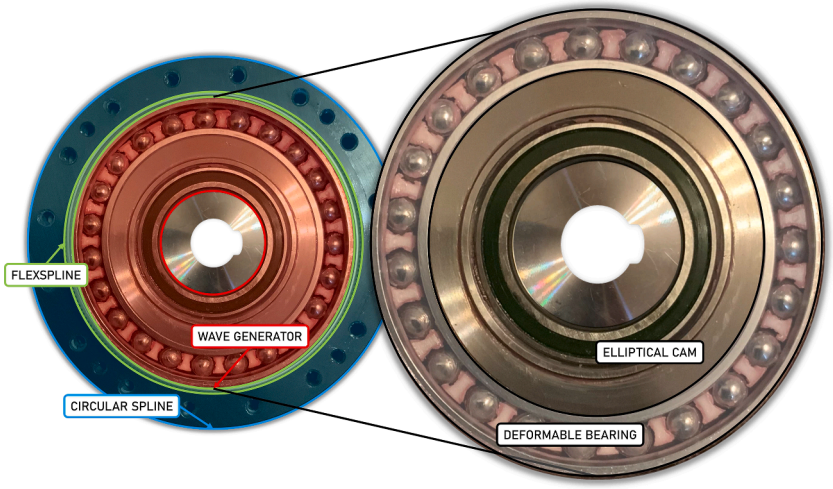

Fig. 1. Harmonid drive reducer components: wave generator (Elliptical cam and deformable bearing), flexspline, and circular spline.

for thin-walled or heavily loaded components. Second, elastic properties introduce compliance and internal damping that shape a transmission's dynamic stiffness, resonance behavior, and positional accuracy; nonlinearities arising from contact geometry, material hysteresis, and friction can produce backlash-like hysteresis, limit cycles, and nontrivial transmissibility effects that rigid or linear models cannot capture. Third, when a bearing's deformation becomes comparable to kinematic clearances or to the operating deflection range, as in many precision reducers, it becomes a key design variable influencing both static performance (e.g., torque capacity and misalignment tolerance) and dynamic behavior (e.g., vibration and control bandwidth). These aspects have long motivated detailed studies of flexible-bearing load distribution and of the coupling between elasticity, contact mechanics, and friction [9,12].

Furthermore, in systems such as harmonic drives in which the deformability of the races is stressed, the bearing represents one of the most critical component and one of the elements most prone to failure [13,14]. Several recent studies have addressed the mechanics and reliability of flexible bearings used in harmonic drives. The subsurface stresses in flexible ball bearings with bendable races has been analyzed in [15] using a superimposition method, highlighting the importance of accurately capturing race deformation. Deformable models also make possible to analyze bearing flexibility to predict fatigue life under cyclic loading. Such simulations help identify stress concentrations and deformation patterns, enabling improved predictive maintenance schedules, component health management, and study of fatigue-related failures, furthermore, this approach enables the integration of model-based Prognostics and Health Management (PHM) methodologies [16].

As aforementioned, the deformable bearing plays a central role in the harmonic drive (or strain-wave) transmission, a compact and precise mechanical reducer used in several applications. It consists of three main components, as shown in Fig. 1: the circular spline (rigid outer ring), the flexspline (thin-walled flexible cup with external teeth), and the wave generator [17]. In most practical designs, the wave generator is realized as a rigid elliptical cam supported by a deformable bearing assembly, so that, as the elliptical cam rotates, the bearing deforms the flexspline locally, engaging the teeth at two lobes and generating the high reduction ratio characteristic of harmonic drives [18]. Because the transmission principle itself relies on controlled elastic deformation of the flexspline and on the compliant interaction at the wave generator/bearing interface, accurate prediction of kinematic error, torque ripple, hysteresis, and fatigue requires explicit modeling of bearing elasticity and internal contact mechanics [19].

Historically, early investigations of bearing performance relied primarily on experimental measurements and empirical description. With advances in theory and computation, these studies evolved toward analytical and later computational models [6]. Classical modeling approaches generally employ simplified representations that capture the bearing's essential behavior while maintaining computational efficiency. They typically include five main categories: lumped-parameter models, quasi-static models, quasi-dynamic models, fully dynamic models, and finite element models (FEMs) [2,20].

A common classical lumped-parameter approach is the rigid-body assumption, in which bearing elements (e.g., inner and outer rings, rolling elements) are considered perfectly rigid [21]. Deformation under load is neglected, and focus is placed on kinematics and contact geometry. This model is valid when deformation is small and has negligible influence on performance or accuracy. However, as accurate as they are [22], it fails to describe systems relying on flexible components, such as those found in harmonic drives.

Another widely used method is the stiffness-matrix approach, which models the bearing as an assembly of springs representing the stiffness of rolling elements and raceways [23]. This method efficiently predicts global stiffness under various loads and misalignments but does not resolve local deformation in detail, especially in elliptical configurations, where deformation is nonuniform.

Classical approach proposed the exploitation of Hertzian theory and elastohydrodynamic lubrication models, contact mechanics analysis remains a key element of bearing modeling. The Hertzian theory, a classical model of contact between curved elastic bodies, provides estimates of contact pressure, deformation, and stress distribution [24]. Elastohydrodynamic lubrication (EHL) models account for the formation of thin lubricant films between rolling elements and raceways, combining surface elasticity with fluid film

behavior to estimate film thickness and friction forces [25]. Although valuable for assessing lubrication and life expectancy, classical EHL formulations assume idealized conditions, such as perfectly smooth surfaces and uniform film thickness, that are seldom realized in deformable bearings.

Despite their usefulness, classical models exhibit several limitations in advanced applications:

- Limited deformability representation: Most assume rigid or simplified elastic behavior, inadequate for the complex deformation seen in bearings used in harmonic drives.
- Neglect of nonlinear and dynamic effects: Static or quasi-static analyses often overlook the nonlinear, time-dependent effects that dominate real systems.
- Simplified contact mechanics: Classical contact models rarely account for surface roughness, localized deformation, or the resulting stress redistribution.
- Computational constraints: While efficient, these models trade accuracy for speed and may lack fidelity for precision applications where flexibility is critical.

For these reasons, in recent years new modelling approaches have been proposed to account for bearing deformability.

The model proposed in [8] couples a semi-analytical formulation with a FEM to describe the deformation of bearing rings and housings. The FEM component accounts for ovalization, torsion, and tulip deformation of the races. However, its weak coupling scheme introduces certain drawbacks: deformation updates are not simultaneous but occur only after several Newton-Raphson iterations of the semi-analytical model. This creates a consistency error which may lead to discrepancies between internal equilibrium and actual geometry, causing numerical instability or slow convergence in highly flexible configurations.

The model also approximates each contact point using a local toroidal surface fitted from nearby FEM nodes. This simplification neglects the global continuity of the deformed ring, treating contacts independently even though ovalization and torsion effects propagate around the circumference. Moreover, the empirical choice of fitting region (disk or sector) can introduce errors or discontinuities, particularly at high contact angles. While the model performs well for four-point contact bearings, it requires toroidal parameterization of the raceways, limiting its applicability to bearings with non-toroidal geometries (e.g., needle rollers or noncircular raceways). A further issue is computational cost: each update requires a separate FEM analysis for both inner and outer rings. Even with a fixed mesh, this approach is far slower than purely semi-analytical models, making it unsuitable for parametric or real-time studies such as multibody simulations or online diagnostics.

Finite element approaches have also been widely employed to investigate the mechanical behavior of flexible bearings. A FEM simulations to analyze load distribution and deformation patterns in harmonic drive flexible bearings is used in [26]. While FEM provides high modeling fidelity, the associated computational cost limits its applicability in parametric studies and system-level simulations.

The model proposed in [27] enables the determination of the contact-force distribution within a rolling bearing subjected to general loading conditions by combining an elasto-static formulation with a Newton-Raphson iterative scheme. The approach employs Hertzian contact theory to describe the local interaction between rolling elements and raceways, while the actual bearing geometry and the applied loads are incorporated into a discrete global structural model. As a result, the method provides consistent estimations not only of the forces acting on each ball but also of the displacements, ring attitude, and evolution of the load zone, achieving good accuracy when compared with FEM-based models while maintaining a significantly lower computational cost. Despite its effectiveness, the model presents several limitations. The formulation is essentially quasi-static and does not account for dynamic, vibrational, or thermo-mechanical effects, which may strongly influence bearing behaviour in high-speed or variable-load applications. Furthermore, it assumes ideal lubrication conditions and neglects key tribological phenomena such as elastohydrodynamic film formation, friction, spin torque, or wear, all of which can affect the real contact-force distribution over time.

Other studies have focused on the structural mechanics of thin-walled flexible bearings. In [28] the static and dynamic mechanical characteristics of harmonic drive flexible bearings has been analyzed using a combination of theoretical modeling and numerical simulations. Their results highlight the importance of accurately capturing ring deformation to predict load distribution. However, the approach relies heavily on numerical simulations and does not provide a computationally efficient model suitable for integration into multibody system simulations.

In [29] a load analysis method for flexible bearings based on a three-force ring superposition approach has been proposed. This method improves the representation of thin-ring deformation effects, but it still relies on simplifying assumptions regarding contact mechanics and does not explicitly model the interaction between individual rolling elements and the deformable races.

Recent works have also addressed the dynamic behavior of flexible bearings in harmonic drive applications. In [12] a dynamic modeling framework for thin-walled elliptical bearings has been proposed, incorporating nonlinear dynamic interactions to study vibration characteristics of harmonic reducers. While this model improves the representation of dynamic behavior, its formulation remains relatively complex and computationally demanding.

Another model is proposed in [14] to study the load distribution on the bearing balls while accounting for the deformability of the bearing races. The authors introduce an improved equivalent-ring formulation, whereas previous literature typically relied on Thin-Walled Ring Theory to model the outer race. This enhanced representation enables the derivation of regression formulas for rapidly estimating ball loads as functions of the bearing's geometric parameters. Moreover, the model allows the analysis of partial contact conditions under high torque levels.

In [30,31] a dynamic model aimed at fault diagnosis of flexible thin-walled bearings in harmonic reducers has been introduced. Their study demonstrates how vibration signatures can be linked to deformation patterns and fault conditions. However, the focus

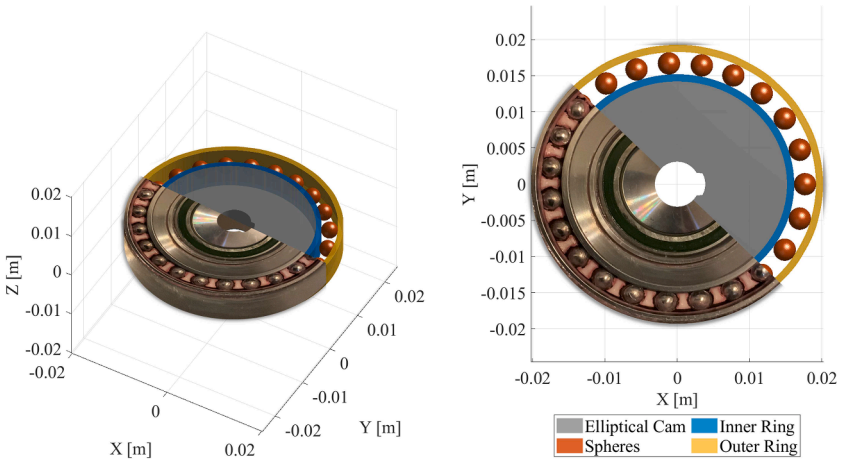

Fig. 2. 3D view of the deformable bearing model.

of the work is primarily on condition monitoring rather than on providing a general mechanical modeling framework suitable for predictive simulations.

Although the progress achieved, modeling deformable bearings in harmonic drive systems remains challenging. Difficulties arise from the multiscale coupling among thin-walled flexspline elasticity and tooth meshing mechanics, local contact deformation and load redistribution within the wave-generator bearing, and nonlinear frictional and hysteretic effects dependent on preload, material properties, and lubrication. The recent numerical and experimental advances have improved load-distribution predictions, fatigue assessment, and dynamic stiffness estimation for thin-walled assemblies, while proposing computationally efficient nonlinear models that capture resonance and compliance behavior [12,32]. Nevertheless, trade-offs persist among model fidelity, parameter identification, and computational cost, particularly when used for design optimization or real-time control. These challenges motivate the modeling approach presented in this paper.

The main objective of the present work is to develop a novel Discrete Flexible Multibody (DFM) bearing model that can be integrated, but not only, into comprehensive harmonic drive simulations.Unlike traditional rigid-body or computationally intensive FEMs, the proposed method represents each bearing ring as a set of interconnected bodies, allowing detailed yet efficient simulation of deformation under load. By balancing accuracy and computational cost, this approach captures nonlinear stiffness, contact mechanics, and dynamic behavior more effectively than classical methods. By embedding the deformable bearing within a larger multibody framework, it becomes possible to study the interaction between the bearing's flexibility, the wave generator, and the flexspline.

The main contributions of this work can be summarized as follows:

- a discrete flexible multibody formulation enabling dynamic simulation of bearings with deformable rings;
- a sector-based representation of the outer ring that captures circumferential coupling while remaining computationally efficient;
- integration of nonlinear contact, friction, and rolling resistance within the multibody formulation;
- reconstruction of the ring deformation through a beam-based homogenization approach suitable for integration into system-level harmonic drive simulations.

2. Mathematical model of the deformable bearing

The present model adopts some simplifying assumptions, including simplified contact laws based on Hertzian theory, and quasi-static beam reconstruction of the outer ring between contact points. These assumptions are consistent with many multibody dynamic formulations and are primarily aimed at preserving computational efficiency. Nevertheless, the proposed framework can be extended to incorporate, among others, more advanced contact and tribological models.

Following the DFM approach the bearing is modeled as a multibody assembly in which the outer ring (race) is represented by a finite number of discrete flexible components (hereafter *sectors*) while rolling elements, cage and inner ring (Fig. 2) are represented as bodies interacting through linear and/or nonlinear contact laws. This strategy captures the coupled rigid-flexible interaction that governs load sharing, contact deflections and the low-frequency structural dynamics of the bearing while keeping the numerical complexity far below a full 3D FEM contact simulation [33].

The rotation of the inner ring, and therefore of its elliptical shape, generates friction tangential forces and shape forces due to the contact between the bearing balls and the races themselves. The balls are modeled both as springs transmitting a normal force from the inner ring to the outer one and as bodies capable of rotating and translating within the raceways.

The force transmitted by the balls causes the outer races to deform. This deformation, as aforementioned, is modeled by dividing the outer raceway into different sectors, each with its own dynamics, subjected to resistive forces aimed at restoring the outer ring to its original shape and maintaining the integrity of the component. By analyzing the deformation of the outer bearing, viewed as a series of supported beams, it is possible to derive the shape of the outer bearing between one contact point and another.

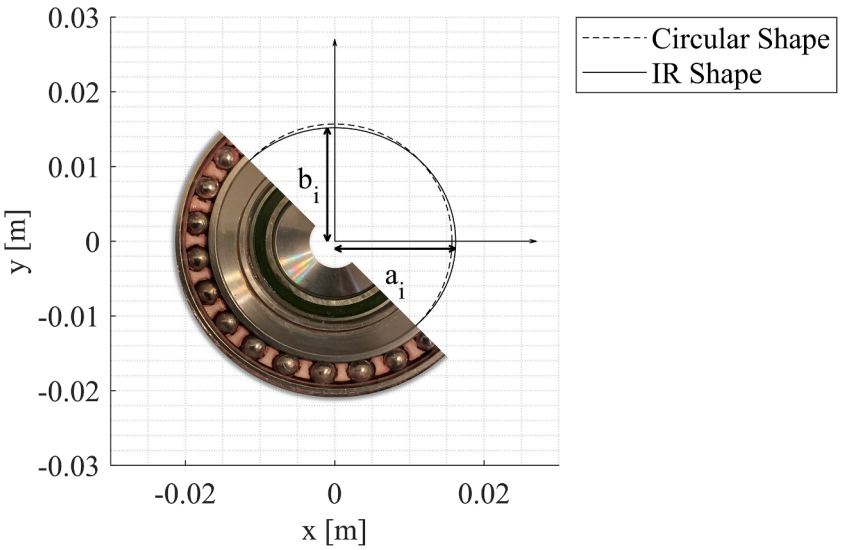

Fig. 3. Bearing deformed inner ring.

The contact between bodies has been modeled as a spring-damper system. A suitable damping term is added in parallel to account for internal dissipation and to suppress high-frequency oscillations that may arise from this relatively stiff interaction [34].

The semi-axes of the inner ring ellipse are calculated by adding and subtracting the deformation (w_0) to the undeformed radius of the inner ring itself (r_{i0}):

$$\begin{aligned} a_i &= r_{i0} + w_0, \\ b_i &= r_{i0} - w_0, \end{aligned} \tag{1}$$

where a_i and b_i are, respectively, the major and minor semi-axis lengths of the elliptical shape (Fig. 3). The detailed modeling of the several interactions, including the force exchange mechanisms and the behavior of each component under deformation, will be described in the following sections.

2.1. Dynamics of the inner ring

The inner ring is modeled as an ideal ellipse, allowing the coordinates of the contact points with the spheres to be obtained kinematically, without the need to implement dynamic equations.

To define the coordinates of the inner ring contact points, a reference coordinate system is first introduced (Fig. 3). For simplicity, the origin is placed at the center of the bearing, while the x and y axes are defined orthogonal to the bearing's rotation axis. The orientation of the bearing in the initial condition is chosen such that the major semi-axis of the ellipse coincides with the x-axis, and the minor semi-axis coincides with the y-axis, as shown in Fig. 3.

2.2. Kinematics of the contact points on the inner ring

With the reference system defined, the coordinates of the contact points on the ellipse representing the inner ring, $(\mathbf{x}_i, \mathbf{y}_i)$, are calculated as follows ("$\circ$" is used to represent the element-by-element Hadamard product):

$$\begin{cases} \mathbf{x}_i = \mathbf{r}_i \circ \cos \boldsymbol{\theta}_i \\ \mathbf{y}_i = \mathbf{r}_i \circ \sin \boldsymbol{\theta}_i \end{cases} \tag{2}$$

Here, $\boldsymbol{\theta}_i$ is the vector of polar angles corresponding to the contact points, while $\mathbf{r}_i$ represents the vector of the deformed inner ring radii, computed as a function of the polar angle:

$$\mathbf{r}_i = \frac{a_i\, b_i}{\sqrt{\left(a_i \sin \boldsymbol{\theta}_i\right)^2 + \left(b_i \cos \boldsymbol{\theta}_i\right)^2}}. \tag{3}$$

The definition of the angular position of the contact points allows the deformation velocity in the radial direction to be obtained as:

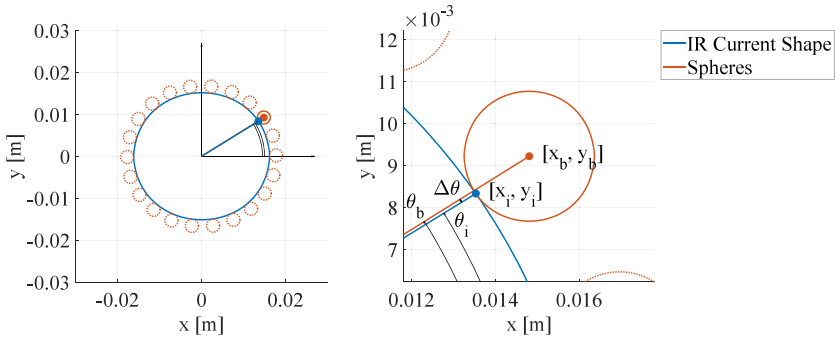

Fig. 4. Difference between the angular positions of the spheres and the contact points.

$$\dot{\mathbf{r}}_{\mathrm{i}} = \omega_{\mathrm{i}} \frac{a_{\mathrm{i}}\, b_{\mathrm{i}} \left(b_{\mathrm{i}}^2 - a_{\mathrm{i}}^2\right) \sin\boldsymbol{\theta}_{\mathrm{i}} \cos\boldsymbol{\theta}_{\mathrm{i}}}{\left[\left(a_{\mathrm{i}} \sin\boldsymbol{\theta}_{\mathrm{i}}\right)^2 + \left(b_{\mathrm{i}} \cos\boldsymbol{\theta}_{\mathrm{i}}\right)^2\right]^{3/2}}. \tag{4}$$

Where ω_{i} is the angular speed of the inner ring. For simplicity in the calculations, the ellipse is assumed with its major semi-axis everytime aligned along the x-axis. To compute the contact point radius eaxh instant an auxiliary angle is therefore introduced as:

$$\boldsymbol{\theta}_{\mathrm{bi}} = \boldsymbol{\theta}_{\mathrm{i}} - \alpha_{\mathrm{i}}. \tag{5}$$

In the undeformed state $\left(a_{\mathrm{i}} = b_{\mathrm{i}}\right)$, the polar position of the contact points coincides with the angle $\boldsymbol{\theta}_{\mathrm{b}}$, which defines the polar position of the sphere centers $\left(\mathbf{x}_{\mathrm{b}}, \mathbf{y}_{\mathrm{b}}\right)$. As the bearing deforms from circular to elliptical, these two angles diverge of a quantity defined as $\Delta\theta$ (Fig. 4), except for the spheres located along the axes.

A correction can be applied to the angular position of the spheres centers to obtain the true angular position of the contact points. Neglecting this correction introduces a systematic error that reaches its maximum when the angular position equals $\pi/4$, and is zero along the axis directions.

A contact point must satisfy two conditions: (i) it must lie on the ellipse, and (ii) the normal to the ellipse at the contact point must pass through the sphere center. The normal versor to the ellipse at the contact point is given by:

$$\hat{\mathbf{n}} = \frac{1}{\sqrt{\left(\frac{a_{\mathrm{i}}}{b_{\mathrm{i}}} \sin\boldsymbol{\theta}_{\mathrm{i}}\right)^2 + \left(\frac{b_{\mathrm{i}}}{a_{\mathrm{i}}} \cos\boldsymbol{\theta}_{\mathrm{i}}\right)^2}} \begin{bmatrix} \frac{b_{\mathrm{i}}}{a_{\mathrm{i}}} \cos\boldsymbol{\theta}_{\mathrm{i}} \\ \frac{a_{\mathrm{i}}}{b_{\mathrm{i}}} \sin\boldsymbol{\theta}_{\mathrm{i}} \end{bmatrix}. \tag{6}$$

Thus, the spheres centers radial coordinates can be expressed as:

$$\mathbf{r}_{\mathrm{b}} = \mathbf{r}_{\mathrm{i}} + r_{\mathrm{s}}\, \hat{\mathbf{n}}. \tag{7}$$

By imposing that the distance between the contact points on the ellipse and the sphere centers equals the sphere radius $\left(r_{\mathrm{s}}\right)$, the following relations can be derived:

$$\begin{cases} x_{\mathrm{b}} = x_{\mathrm{i}} + r_{\mathrm{s}}\, \hat{n}_x = r_{\mathrm{i}} \cos\boldsymbol{\theta}_{\mathrm{i}} + r_{\mathrm{s}} \dfrac{b_{\mathrm{i}} \cos\boldsymbol{\theta}_{\mathrm{i}}}{a_{\mathrm{i}} \sqrt{\left(\frac{a_{\mathrm{i}}}{b_{\mathrm{i}}} \sin\boldsymbol{\theta}_{\mathrm{i}}\right)^2 + \left(\frac{b_{\mathrm{i}}}{a_{\mathrm{i}}} \cos\boldsymbol{\theta}_{\mathrm{i}}\right)^2}} \\ y_{\mathrm{b}} = y_{\mathrm{i}} + r_{\mathrm{s}}\, \hat{n}_y = r_{\mathrm{i}} \sin\boldsymbol{\theta}_{\mathrm{i}} + r_{\mathrm{s}} \dfrac{a_{\mathrm{i}} \sin\boldsymbol{\theta}_{\mathrm{i}}}{b_{\mathrm{i}} \sqrt{\left(\frac{a_{\mathrm{i}}}{b_{\mathrm{i}}} \sin\boldsymbol{\theta}_{\mathrm{i}}\right)^2 + \left(\frac{b_{\mathrm{i}}}{a_{\mathrm{i}}} \cos\boldsymbol{\theta}_{\mathrm{i}}\right)^2}} \end{cases}. \tag{8}$$

This leads to the following expression relating the angular positions:

$$\tan\boldsymbol{\theta}_{\mathrm{b}} = \frac{y_{\mathrm{b}}}{x_{\mathrm{b}}} = Q\left(\theta_{\mathrm{i}}\right) \frac{\sin\boldsymbol{\theta}_{\mathrm{i}}}{\cos\boldsymbol{\theta}_{\mathrm{i}}} = Q\left(\theta_{\mathrm{i}}\right) \tan\boldsymbol{\theta}_{\mathrm{i}}; \tag{9}$$

with:

$$Q(\theta_i) = \frac{r_i + \dfrac{r_s\, a_i}{b_i \sqrt{\left(\frac{a_i}{b_i}\sin\theta_i\right)^2 + \left(\frac{b_i}{a_i}\cos\theta_i\right)^2}}}{r_i + \dfrac{r_s\, b_i}{a_i \sqrt{\left(\frac{a_i}{b_i}\sin\theta_i\right)^2 + \left(\frac{b_i}{a_i}\cos\theta_i\right)^2}}} \tag{10}$$

for small ball radius it is possible to write the first expansion of the term respect to the radius itself:

$$Q(\theta_i) = 1 + r_s \frac{a_i^2 - b_i^2}{a_i b_i r_i \sqrt{\left(\frac{a_i}{b_i}\sin\theta_i\right)^2 + \left(\frac{b_i}{a_i}\cos\theta_i\right)^2}} + O(r_s^2). \tag{11}$$

Analysing this expression it is possible to observe that if $a_i = b_i$, i.e. the undeformed condition, the error is null because the ball centers positions are equal to the inner ring contact points angular positions. Assuming the error is small, the angular difference can be approximated by:

$$\Delta\theta = \theta_i - \theta_b \approx \frac{r_s\left(a_i^2 - b_i^2\right)}{a_i\, b_i\, r_i \sqrt{\left(\frac{a_i}{b_i}\sin\theta_i\right)^2 + \left(\frac{b_i}{a_i}\cos\theta_i\right)^2}} \frac{\sin 2\theta_b}{2}. \tag{12}$$

This term quantifies how much the direction of the sphere centers (assumed equal to the intersection point direction) deviates from the true direction of the contact point on the ellipse. The angular error has a symmetric shape proportional to $\sin 2\theta_b$, vanishing each 90° and peaking each 45°. Therefore, a correction of the form:

$$\theta_i \approx \theta_b - k_{ellip,0}\, \sin 2\theta_b; \tag{13}$$

reduces the first-order error, where the constant $k_{ellip,0}$ represents the amplitude of the dominant harmonic component. This correction is effective for small eccentricities; for larger eccentricities or bigger spheres, higher-order harmonics must be considered.

From the perturbative expansion, the correction constant can be expressed as:

$$k_{ellip} = \frac{r_s\left(a_i^2 - b_i^2\right)\sqrt{\left(a_i\sin\theta_i\right)^2 + \left(b_i\cos\theta_i\right)^2}}{2\, a_i^2\, b_i^2 \sqrt{\left(\frac{a_i}{b_i}\sin\theta_i\right)^2 + \left(\frac{b_i}{a_i}\cos\theta_i\right)^2}}. \tag{14}$$

The maximum correction factor used in the model is:

$$k_{ellip,0} = \frac{2\, r_s\, r_{i0}\, w_0 \sqrt{r_{i0}^2 + w_0^2}}{(r_{i0}^2 - w_0^2)\sqrt{r_{i0}^4 + 6\, r_{i0}^2\, w_0^2 + w_0^4}} \approx 2\,\frac{r_s\, w_0}{r_{i0}^2}. \tag{15}$$

This formula highlights the factors controlling the angular error:

- it is proportional to the eccentricity parameter w_0;
- it is proportional to the sphere radius r_s.

In Fig. 5 it is possible to observe the error caused using the angular position of the spheres center in place of the angular position of the contact points againt to the correction proposed.

From the analysis of the correction factor, two limiting conditions can be identified: (i) when the sphere radius tends to zero (no balls), the sphere centers coincide with the inner ring shape; and (ii) when the eccentricity is null (circular bearing), the correction vanishes, since the angular position of the sphere centers matches that of the contact points.

In Fig. 6 the position of the contact points between the spheres and the inner ring (blue markers) have been shown.

2.3. Bearing Hertzian contact forces

From the perspective of the force exchanged through the bearings, each sphere is modeled as a spring-damper system (Fig. 7), so a damping force is also included to account for material dissipation, but it is not reported in the math expression for simplicity. The modulus of the force is determined by applying Hertzian contact theory, resulting in the following expression:

$$\mathbf{F}_b = h\,\mathbf{k}_b \circ \boldsymbol{\delta}_{b,\perp}^{\gamma_b}; \tag{16}$$

where:

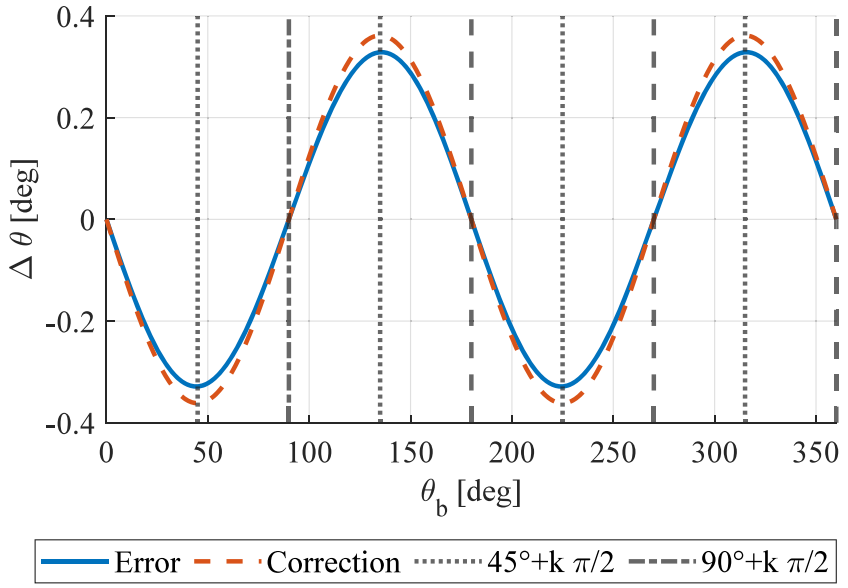

Fig. 5. Difference between spheres angular position and conctact points angular position against to angular correction.

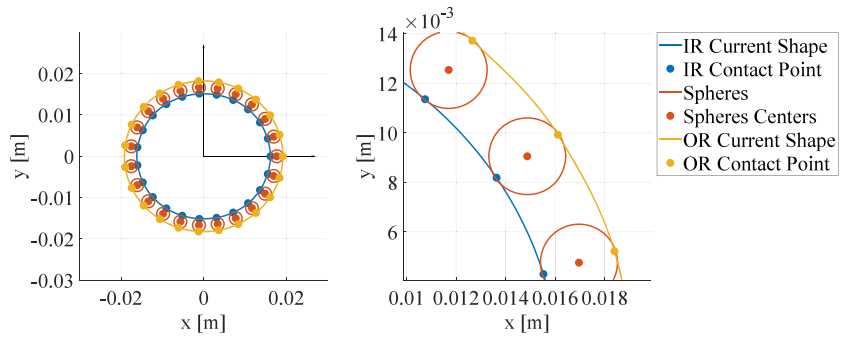

Fig. 6. Contact points and shapes of inner ring and outer ring.

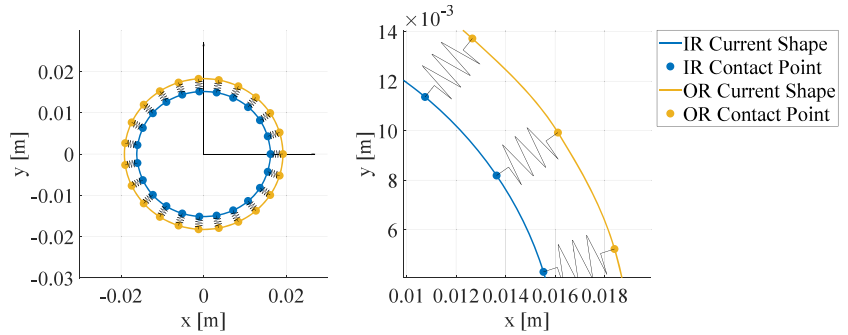

Fig. 7. Spheres spring model.

- h is a function ensuring that the force acts only in compression;
- $\mathbf{k}_b$ is the vector stiffnesses of the sphere;
- $\boldsymbol{\delta}_{b,\perp}$ is the vector representing the sphere compression or “dilatation” relative to its undeformed condition;
- γ_b is the bearing force exponent, which for ball bearings is equal to $\frac{3}{2}$.

To compute the compression, it is necessary to calculate the distance between the contact points on the inner and outer rings. This distance is then subtracted by the sphere diameter in its undeformed condition. As mentioned earlier, in a real bearing the sphere can only be subjected to compression. If the two rings separate by a distance greater than the diameter of the sphere, detachment occurs

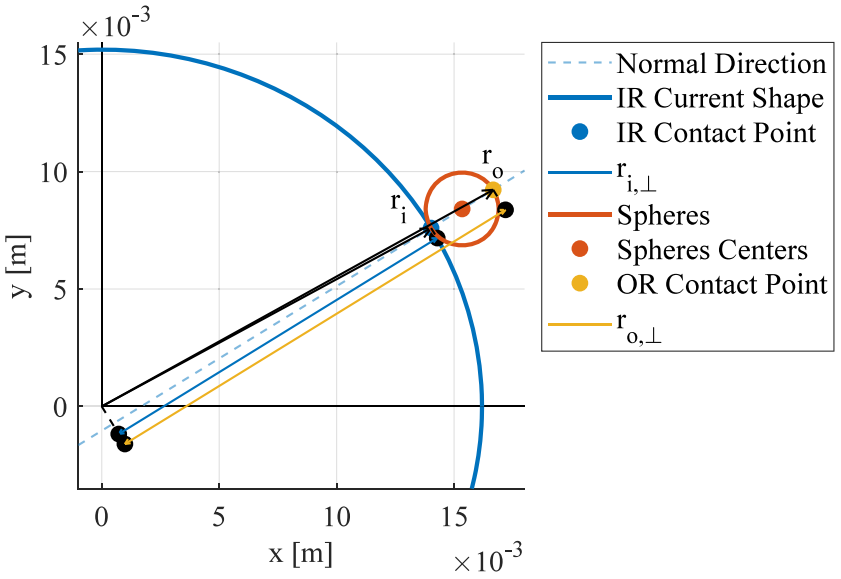

Fig. 8. Contact points on the inner ring and outer ring radius coordinates on elliptical shape normal direction.

between the sphere and one of the races. Therefore, it is essential to incorporate the function $h(\delta_b)$ into the calculation of the force in order to effectively excludes tensile forces arising from race separation by setting the contact force to zero.

$$h(\delta_b) = \begin{cases} 1, & \delta_b < 0, \\ 0, & \delta_b \geq 0, \end{cases} \tag{17}$$

The Hertzian contact theory is applied to determine the radial stiffness values of individual bearing balls (k_b), considering the elliptical contact region formed between the ball and the raceways. According to [35], obtaining an analytical solution for the parameters that describe the contact surface is not possible. Therefore, a numerical method originally developed by Hamrock and Anderson [1] and later refined by Guay and Frikha is employed.

The radii coordinates of the inner and outer ring contact points, due to the deformation, are not aligned along the radius direction, as shown in Fig. 8. Therefore, it is necessary to calculate the spheres "compression" in the normal direction:

$$\boldsymbol{\delta}_{b,\perp} = \left(\mathbf{r}_{o,\perp} - \mathbf{r}_{i,\perp}\right) - 2\,r_s; \tag{18}$$

Where $\mathbf{r}_o$ is the vector of the radius coordinate of the contact points on the outer ring and $\mathbf{r}_{i,\perp}$ is the normal component of the radius coordinate of the contact point on the inner ring, calculated as:

$$\mathbf{r}_{i,\perp} = \frac{a\,b\sqrt{\left(a_i\,\sin\theta_i\right)^2 + \left(b_i\,\cos\theta_i\right)^2}}{\sqrt{\left(a_i^2\,\sin\theta_i\right)^2 + \left(b_i^2\,\cos\theta_i\right)^2}}. \tag{19}$$

Observing the graph in Fig. 9, it is possible to notice how the largest forces are aligned with the major axes and the smallest with the minor axes. This behaviour is clearly explained by the fact that the local normal deflection of each sphere-raceway contact depends on the angular position of the elliptical shape, i.e. the angular position of the inner ring.

When a ball lies close to the major axis, the normal indentation is maximised and therefore there is a higher Hertzian contact force. Conversely, balls located near the minor axis experience a much smaller indentation (almost null) and hence smaller contact forces.

This distribution, a direct consequence of the elliptical deformation, leads to a non-uniform radial displacement around the raceway, which in turn modulates the local contact load according to the relative angular position of each sphere.

It should be noted that the classical Hertzian contact formulation assumes interaction between bodies that can be approximated as semi-infinite elastic solids. In harmonic drive bearings the outer race is typically a thin-walled component, which may partially violate this assumption. In the present model, Hertzian contact is adopted as a first-order approximation because it provides a computationally efficient representation of rolling-element contact mechanics and is widely used in dynamic bearing models [35]. The contact indentation depth remains significantly smaller than the race thickness, which allows the Hertzian approximation to remain acceptable for system-level simulations. Nevertheless, thin-wall effects may influence the local stress distribution, and more refined contact models or FEM-based corrections could be introduced in future developments to further improve the accuracy of the contact formulation.

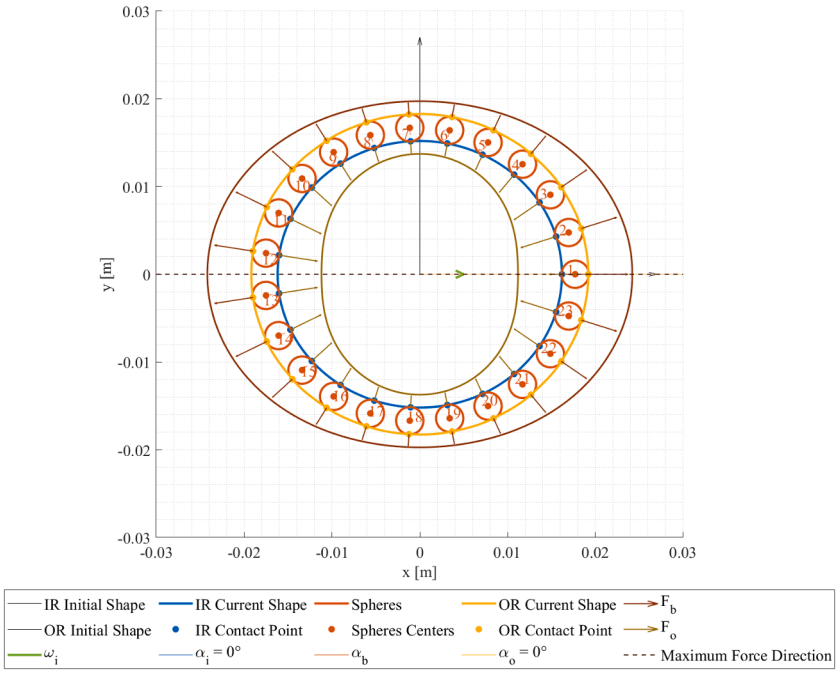

Fig. 9. Representation of the static configuration of the deformable bearing keyed on the elliptical cam.

2.4. Outer ring homogenization and anchoring forces

In the undeformed configuration, each segment of the outer ring between two adjacent contact points can be represented as a circular arc of radius:

$$r_{o0} = r_{i0} + 2\,r_s; \tag{20}$$

corresponding to the nominal radius of the ring in the unloaded condition.

During deformation, the distance between two adjacent sectors on the race of the bearing deviates from its nominal circular configuration. This variation gives rise to interaction forces both between neighboring sectors and within each individual sector.

To describe this behavior, two distinct force components are defined for each sector. A sector (Fig. 10) is considered as a portion of the outer ring surrounding a contact point; it is not geometrically fixed but dynamically defined around the contact points along the circumferential direction. The two ends of a sector are defined as the middle points between two contact points. The total force acting on a contact point, arising from the ring's sectoral behavior, can therefore be expressed as:

$$\mathbf{F}_o = \mathbf{F}_{o,h} + \mathbf{F}_{o,a}. \tag{21}$$

$$\begin{aligned} F_{o,h}(i) &= k_h \left[r_{o,\perp}(i-1) + r_{o,\perp}(i+1) - 2\,r_{o,\perp}(i) \right]; \\ & \qquad\qquad i = 1, \ldots, N_b. \\ F_{o,a}(i) &= k_a \left[r_{o,\perp}(i) - k_{pl}\, r_{o0} \right]. \end{aligned} \tag{22}$$

The first term, referred to as the homogenization force (or coupling force), tends to even out the differences in radius between adjacent sectors. The homogenization force represents the discrete counterpart of the circumferential elastic coupling of a thin circular ring. In the continuous formulation of thin-ring mechanics, the radial deformation varies along the circumferential coordinate and the associated bending response depends on the spatial curvature of the deformation field, which is proportional to the second derivative $\partial^2 r / \partial \theta^2$ [36,37].

When the ring is discretized into a finite number of circumferential sectors, this operator can be approximated through a central finite-difference formulation, yielding expressions of the form $r_{i+1} - 2r_i + r_{i-1}$. The resulting term therefore corresponds to the discrete Laplacian operator along the ring circumference.

An equivalent interpretation can also be obtained from an energy-based formulation in which the circumferential non-uniformity of the radial displacement is penalized through a quadratic elastic energy proportional to $(r_{i+1} - r_i)^2$. Taking the gradient of this energy with respect to the sector displacement naturally leads to the coupling force $F_{o,h}(i) = k_h(r_{i-1} + r_{i+1} - 2r_i)$. This approach preserves the essential mechanical coupling between adjacent sectors while remaining compatible with multibody dynamic simulations.

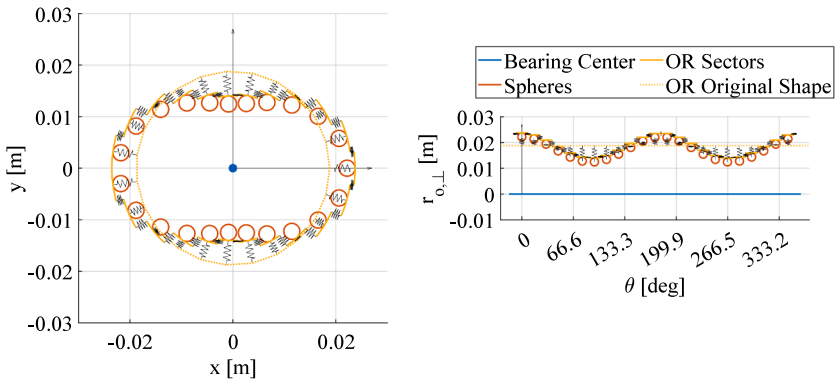

Fig. 10. Spring model used to represent the coupling between adjacent outer-ring sectors (circular and linearized configuration). For illustrative clarity, the radial offsets between sectors are intentionally magnified.

The second term, referred to as the anchoring force, acts to restore each sector to its undeformed configuration, corresponding to a perfectly circular ring with a radius equal to r_{o0}. It arises from the overall stiffness of the ring material, which resists circumferential expansion. Hence, this force has a local character, acting on each sector according to its deviation from the nominal geometry. This contribution includes both membrane effects (circumferential elongation that tends to restore the original circumference) and local bending due to curvature.

The parameter k_{pl} denotes the preload factor, ensuring that the rolling elements remain in contact even in the absence of external load. After assembly, the outer ring is effectively "forced" into a geometry with a slightly smaller radius than its natural, stress-free configuration. This geometric constraint induces a static compressive state in the system: the ring tends to contract, while the balls oppose this motion. As a consequence, a nonzero internal pressure develops at the ball-raceway contacts even at rest, providing the desired preload.

As shown in Fig. 9, it is possible to observe that the pattern of the sector forces is similar and essentially the mirror image of the bearing-force distribution. This behaviour is expected in a balanced configuration, where the deformation of the ring and the reaction forces in each sector must oppose the ball-raceway contact forces, restoring equilibrium.

2.5. *Friction forces between the spheres and the races*

The interaction between each sphere and the two races is governed by frictional forces that induce both translational and rotational motion of the spheres, as well as sliding between the rolling elements and the two rings, similarly to the approach adopted in [38] for modeling ball-race contact in the ball screw system. To correctly evaluate these forces, it is first necessary to define the relative slip velocities at each contact interface.

$$\mathbf{v}_{\text{slip,i}} = \mathbf{v}_{\text{i}} - \left(\mathbf{v}_{\text{b}} - \boldsymbol{\omega}_{\text{b}}\, r_{\text{s}}\right); \qquad \mathbf{v}_{\text{slip,o}} = \mathbf{v}_{\text{o}} - \left(\mathbf{v}_{\text{b}} + \boldsymbol{\omega}_{\text{b}}\, r_{\text{s}}\right). \tag{23}$$

Here, $\mathbf{v}_{\text{i}} = \boldsymbol{\omega}_{\text{i}} \circ \mathbf{r}_{\text{i},\perp}$ and $\mathbf{v}_{\text{o}} = \boldsymbol{\omega}_{\text{o}} \circ \mathbf{r}_{\text{o},\perp}$ denote, respectively, the tangential velocities of the contact points on the inner and outer rings; $\mathbf{v}_{\text{b}}$ is the tangential velocity of the sphere centers, and $\boldsymbol{\omega}_{\text{b}}$ is the angular velocity of the spheres around their centers.

The normal (compressive) contact force $\mathbf{F}_{\text{b}}$ acts along the line joining the contact points on the surfaces. From this quantity and the friction coefficients, the tangential friction forces at the two contact interfaces can be expressed as:

$$\mathbf{F}_{\mu,\text{i}} = \mathbf{F}_{\text{b}} \circ \boldsymbol{\mu}_{\text{i}}(v_{\text{slip,i}}); \qquad \mathbf{F}_{\mu,\text{o}} = \mathbf{F}_{\text{b}} \circ \boldsymbol{\mu}_{\text{o}}(v_{\text{slip,o}}). \tag{24}$$

The friction coefficient between lubricated metallic contacts can be effectively represented by the Stribeck model [39], which describes the transition between boundary, mixed, and hydrodynamic lubrication regimes as a function of the relative sliding velocity (Fig. 11). In a rolling-sliding contact such as a steel ball compressed between two steel races, the model captures the typical decrease of friction with increasing velocity due to the formation of a lubricating film [40].

The exploited continuous and differentiable formulation of the Stribeck curve, suitable for dynamic simulations, can be expressed as:

$$\mu = \left[\mu_{\text{C}} + (\mu_{\text{s}} - \mu_{\text{C}})\, e^{-\left|v_{\text{slip}}/v_{\text{S}}\right|^2}\right] \tanh\left(\frac{v_{\text{slip}}}{v_{\epsilon}}\right) + k_{\mu}\, v_{\text{slip}}. \tag{25}$$

where:

- μ_{s} is the static (or boundary) friction coefficient, corresponding to very low velocities where asperity contact dominates;
- μ_{C} is the Coulomb (or kinetic) friction coefficient, representing the steady-state value in the mixed or elastohydrodynamic regime;

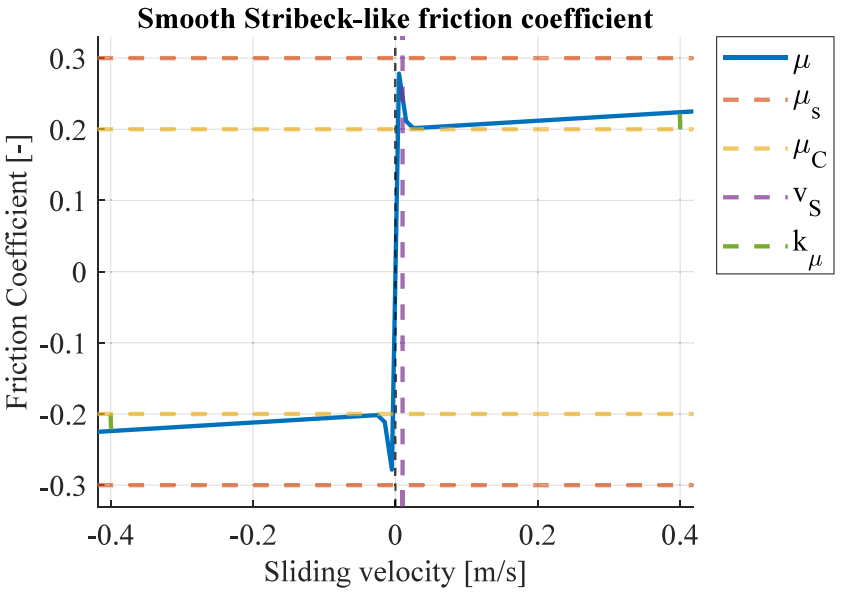

Fig. 11. Friction coefficient as a function of the sliding speed.

- v_S is the Stribeck characteristic velocity, which controls the decay rate from μ_s to μ_C and marks the approximate transition between boundary and mixed lubrication regimes;
- v_ε is a small regularization velocity that ensures numerical smoothness and introduces the velocity sign in a continuous manner;
- k_μ is the viscous friction coefficient, accounting for the linear viscous contribution that becomes significant at high sliding velocities in the hydrodynamic regime [41].

The parameters μ_s, μ_C, and v_S depend primarily on the lubricant viscosity, the normal load, and the surface roughness. The exponential term ensures a smooth decay from the boundary to the mixed lubrication regime, while the hyperbolic tangent provides a symmetric and continuous behavior around zero velocity. Compared to more complex dynamic friction models (e.g., LuGre or Leuven), the Stribeck formulation offers a good compromise between physical accuracy and numerical efficiency, making it well suited for simulations of lubricated rolling contacts [42–44].

2.6. Dynamics and kinematics of the contact points on the outer ring

The dynamics of the contact points on the outer ring must be analyzed both in the normal direction, to evaluate the bearing reaction forces, and in the tangential direction, to study the sliding and frictional interaction between the spheres and the outer ring.

Each contact point between a sphere and the outer ring lies along the direction normal to the local ellipse profile. Its position in the normal direction is obtained from a dynamic equilibrium between the normal force transmitted through the spheres $(\mathbf{F}_b)$, the homogenization and anchoring forces acting on the outer ring $(\mathbf{F}_o)$, and the equivalent forces vector from the external load $(\mathbf{Q}_t)$:

$$\mathbf{F}_b + \mathbf{F}_o - \mathbf{Q}_t = \mathbf{m}_a \circ \ddot{\mathbf{r}}_{o,\perp}. \tag{26}$$

Here, $\mathbf{m}_a$ denotes the mass vector associated with the oth sector of the outer ring $(\mathbf{m}_o)$ and the bth sphere $(\mathbf{m}_b)$. The total mass of the ring (Mo) is assumed to be uniformly distributed among all sectors (N_o), which coincide with the number of rolling elements (N_b). In future developments, a non-uniform mass distribution may be introduced in order to investigate unbalanced configurations and possible mounting-error effects. To simplify the numerical solution of the dynamic equations, the mass was increased so that the system's natural frequency is at least one order of magnitude higher than the excitation frequency associated with the maximum rotational speed of the input shaft.

As previously discussed, the variable $r_{o,\perp}$ does not represent the absolute radial coordinate of the outer ring contact points with respect to the bearing center; instead, it describes their displacement along the local normal direction (Fig. 8). The actual Cartesian $(\mathbf{x}_o, \mathbf{y}_o)$, hence polar $(\theta_o, \mathbf{r}_o)$, coordinates of the outer ring contact points can be obtained by projecting this normal displacement onto the global reference frame (Fig. 12).

$$\begin{cases} \theta_o \approx \theta_b + k_{ellip,0} \sin 2\theta_b \\ \mathbf{r}_o = \mathbf{r}_{o,\perp} \dfrac{\sqrt{\left(a_i^2 \sin\theta_i\right)^2 + \left(b_i^2 \cos\theta_i\right)^2}}{a_i^2 \sin\theta_i \circ \sin\theta_o + b_i^2 \cos\theta_i \circ \cos\theta_o} \end{cases}. \tag{27}$$

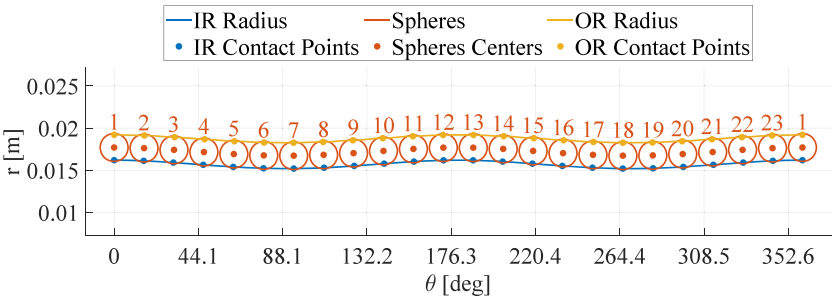

Fig. 12. Radii of the inner and outer rings in the deformed configuration.

From the above expression, it can be observed that when the eccentricity is zero (i.e., when the ellipse degenerates into a circle), the position of the outer ring contact points reduces to $(\theta_o = \theta_b,\ \mathbf{r}_o = \mathbf{r}_{o,\perp})$, as expected for a circular bearing configuration.

To quantify the slip velocity between the spheres and the outer ring, it is necessary to determine the tangential velocity of the contact points. The tangential motion of each outer ring sector can be obtained from the translational dynamic equilibrium along the tangential direction. Considering the free-body diagram and assuming that all forces act at the contact point, the tangential equilibrium is expressed as:

$$\mathbf{F}_{\mu,o} - \mathbf{F}_{c,o} - \mathbf{C}_o = \mathbf{m}_o \circ \dot{\mathbf{v}}_o; \tag{28}$$

where $\mathbf{F}_{\mu,o}$, as described in Section 2.5, is the tangential friction force acting between the sphere and the outer race, $\mathbf{v}_o$ is the tangetial speed of the sectors, $\mathbf{F}_{c,o}$ is the viscous friction acting on the outer ring due to external factors like air resistance, and $\mathbf{C}_o$ is the constraint force defined to impose no rotation on the ring in order to simulate the presence of the flexspline or the configuration of a possible test bench.

2.7. Cage interaction forces between adjacent spheres

In order to model the cage interaction, each ball is coupled to its two adjacent neighbors through angular spring-like forces. The purpose of these interaction forces is to maintain the angular separation between consecutive ball centers close to the ideal value equal to:

$$\Delta\theta_0 = \frac{2\pi}{N_b}. \tag{29}$$

For each sphere, two interaction forces can be introduced: one due to the next ball in the sequence and one due to the previous ball. These forces are defined as:

$$\begin{aligned} F_{c,i+1}(i) &= k_c \left[\theta_i(i+1) - \left(\theta_i(i) + \Delta\theta_0\right)\right], \\ & \qquad i = 1, \ldots, N_b. \\ F_{c,i-1}(i) &= k_c \left[\theta_i(i-1) - \left(\theta_i(i) - \Delta\theta_0\right)\right]. \end{aligned} \tag{30}$$

where k_c is the angular stiffness associated with the cage-ball interaction. The sign convention ensures that the force becomes repulsive when two balls move too close and attractive when the spacing increases beyond the nominal value. The total generalized force acting on the ith ball due to the cage is therefore

$$F_c(i) = k_c \left[\theta_i(i+1) + \theta_i(i-1) - 2\,\theta_i(i)\right], \quad i = 1, \ldots, N_b. \tag{31}$$

This expression corresponds to a discrete angular Laplacian, which naturally promotes uniform spacing of the balls along the raceway (Fig. 13).

2.8. Rolling resistance modelling

The rolling resistance (or rolling friction) is the torque opposing the rolling motion of a sphere or wheel on a surface. Physically, it originates from the hysteresis of the contacting materials, the microscopic slip at the contact patch, and from viscous effects due to surface lubrication [45]. Unlike Coulomb or sliding friction, which directly resists tangential translation, rolling resistance manifests as a torque that dissipates mechanical energy even when pure rolling is nearly maintained.

Several models have been proposed in literature to describe rolling resistance with different levels of complexity: Constant Torque Model [46], Hertzian-Geometric Model [47,48], Viscoelastic Models [49], and Hertz-Dissipative Models.

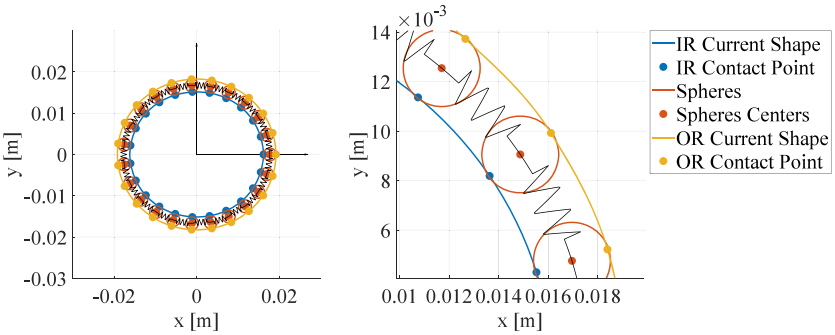

Fig. 13. Cage spring model.

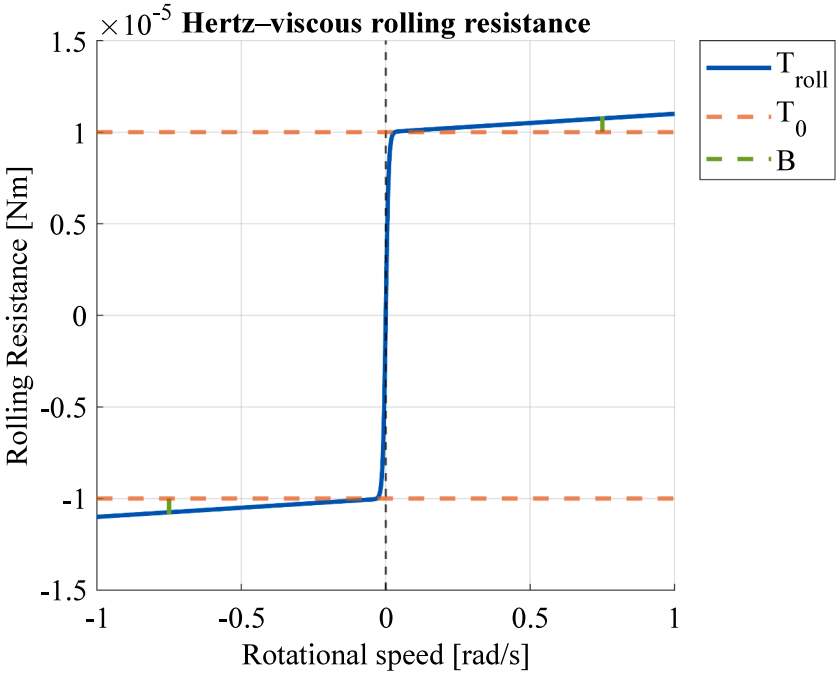

Fig. 14. Rolling resistance torque as a function of the rotational speed.

In this work, the last approuch is implemented by means of a continuous formulation (Fig. 14), expressed as:

$$\mathbf{T}_{\text{roll}} = T_0 \tanh\left(\frac{\boldsymbol{\omega}_{\text{b}}}{\omega_{\text{s}}}\right) + B\,\boldsymbol{\omega}_{\text{b}}; \tag{32}$$

where:

- T_{roll} is the rolling resistance torque opposing the relative angular velocity;
- ω_{b} is the angular velocity of a sphere;
- T_0 represents the quasi-static or elastic hysteresis component of the torque (“dry” rolling resistance);
- ω_{s} is a smoothing parameter controlling the transition from the static to the dynamic regime;
- B is a viscous coefficient accounting for viscoelastic and lubrication effects.

The hyperbolic tangent ensures that the torque is continuous and differentiable for all ω_{b}, avoiding numerical discontinuities at zero velocity while preserving a physically realistic saturation. Moreover, the torque automatically vanishes when no rotational motion is present, satisfying the physical requirement of zero resistance under static equilibrium.

This formulation provides a physically consistent and numerically robust representation of rolling resistance, suitable for the studied implementation.

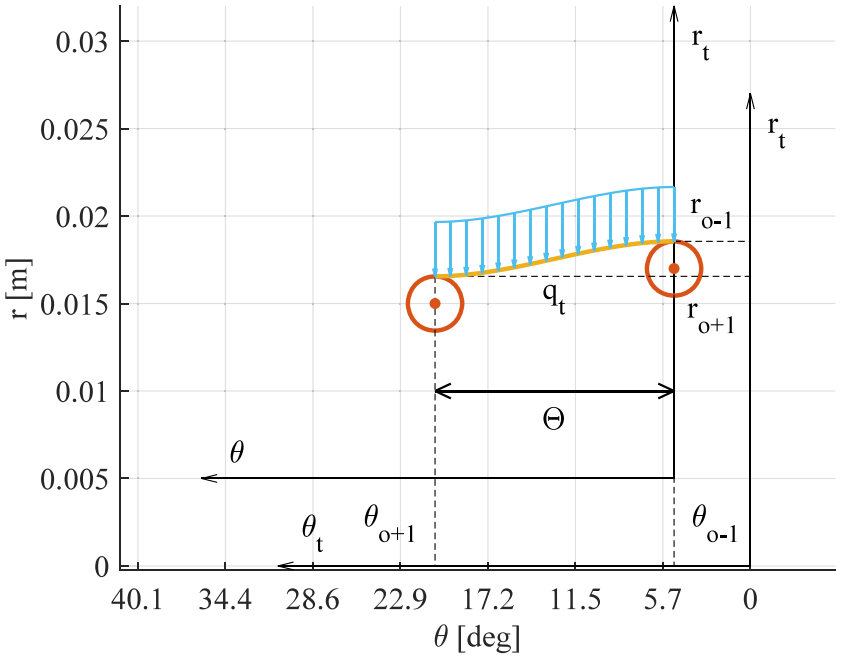

Fig. 15. Diagram of a beam-like sector of the outer ring.

2.9. Dynamics of the spheres

As in previous bearing models available in the literature, the rolling elements (the spheres) are represented as massless springs in the normal direction. However, since the instantaneous position of each sphere along the elliptical path must be determined, both its rotational and tangential dynamics must be explicitly included.

These two motions are treated separately because slip between the spheres and the races may occur. The dynamics of each sphere are described by the following set of vectorial equations:

$$\begin{cases} \mathbf{F}_{\mu,\mathrm{i}} + \mathbf{F}_{\mu,\mathrm{o}} + \mathbf{F}_{\mathrm{c}} = \mathbf{m}_{\mathrm{b}} \circ \dot{\mathbf{v}}_{\mathrm{b}} = \mathbf{m}_{\mathrm{b}} \circ \ddot{\boldsymbol{\theta}}_{\mathrm{b}} \circ \mathbf{r}_{\mathrm{b},\perp} \\ \left(\mathbf{F}_{\mu,\mathrm{i}} - \mathbf{F}_{\mu,\mathrm{o}}\right) \circ \mathbf{r}_{\mathrm{s}} - \mathbf{T}_{\mathrm{roll}} = \mathbf{I}_{\mathrm{b}} \circ \dot{\boldsymbol{\omega}}_{\mathrm{b}} = \mathbf{I}_{\mathrm{b}} \circ \ddot{\boldsymbol{\alpha}}_{\mathrm{b}} \end{cases} . \tag{33}$$

where $\mathbf{r}_{\mathrm{b},\perp}$ is the radial coordinate of the sphere center, defined as the mean of the inner and outer ring normal contact radii:

$$\mathbf{r}_{\mathrm{b},\perp} = \frac{\mathbf{r}_{\mathrm{i},\perp} + \mathbf{r}_{\mathrm{o},\perp}}{2}. \tag{34}$$

2.10. Deformation of the outer ring between contact points

The calculations presented so far have focused exclusively on the contact points between the spheres and the races. In this section, the deformation of the outer ring between each pair of contact points is analyzed in order to describe the mechanical response of the entire bearing structure under load.

As aforementioned the outer ring is discretized into N_{b} circumferential sectors, each associated with a contact point with a rolling element. The normal displacement of each contact point is obtained from the dynamic equilibrium between the contact forces transmitted by the spheres, the homogenization forces (which account for circumferential coupling), and the anchoring forces (which restore the undeformed configuration).

During deformation, the radii at the contact points differ from the undeformed radius and from each other. To capture this behavior, the outer ring is discretized into N_{o} beam-like sectors (different from sectors used in the outer ring dynamic description and for this reason simple called *beams*), each extending from one contact point to the next. For each beam, the first contact point $\left(\theta_{\mathrm{o}}(i) = \theta_{\mathrm{o\text{-}1}}\right)$ is included from the discretization, while the second $\left(\theta_{\mathrm{o}}(i+1) = \theta_{\mathrm{o}+1}\right)$ is excluded. This avoids double counting of nodes shared between adjacent beams. Furthermore it is necessary to consider a wrap-around boundary conditions, i.e., the first “beam” is connected to the last one to ensure geometrical continuity.

The deformation of the ring between adjacent contact points is then reconstructed using an equivalent beam formulation [50]. Each segment is modeled as an Euler-Bernoulli beam subjected to a distributed load, with boundary conditions imposed at the contact points. This allows a continuous deformation profile to be obtained while preserving compatibility between neighboring sectors.

Each beam (Fig. 15) is described by means of absolute coordinate defined as θ_t and single beam relative coordinate defined as $\theta = \theta_t - \theta_{o-1}$, beam angular length $\Theta = \theta_{o+1} - \theta_{o-1}$ and subjected to a distributed load per unit length, $q_t(\theta)$, representing external forces on the ring.

The load redistribution mechanism is inherently captured by the coupling between adjacent sectors through the homogenization term, which acts as a discrete approximation of the circumferential bending stiffness of the ring. As a result, local variations in contact forces are propagated along the ring, leading to a physically consistent redistribution of deformation and load. This procedure ensures that the global ring response remains continuous and mechanically coherent while maintaining a computationally efficient formulation suitable for multibody simulations.

To characterize the behavior of a single beam, a quasi-static formulation was adopted. This choice is not motivated by slow joint motion, but due to the rapid dynamic response of the system, as the outer ring constitutes the least rigid component of the assembly. Although the distributed load and the contact points radii may vary with time, the beam is assumed to adapt instantaneously.

The differential equation governing the transverse deflection $\left(\mathbf{r}_t(\theta)\right)$ is:

$$q_t(\theta) = E\, I_o \frac{\mathrm{d}^4 r_t}{\mathrm{d}\left(r_o\, \theta\right)^4} \approx \frac{E\, I_o}{r_o^4} \frac{\mathrm{d}^4 r_t}{\mathrm{d}\theta^4}, \tag{35}$$

The general solution can be written as a cubic polynomial plus a particular solution $\left(r_{t,P}\right)$ associated with the applied load:

$$r_t(\theta) = A_0 + A_1\, \theta + A_2\, \theta^2 + A_3\, \theta^3 + r_{t,P}, \tag{36}$$

The load is approximated by assuming a constant distributed load over each beam, defined as the average of the loads acting on the sub-elements within that sector. The outer ring is discretized into N_t elements, each exerting a load on the ring. Depending on their angular position, these elements may or may not belong to a given sector. A smooth engaging function $\left(\mathbf{h}_t\right)$ based on a hyperbolic tangents is used to assign each element to a beam. This beam assignment is also employed to compute the external load acting on the spheres $\left(\mathbf{Q}_t\right)$, with contributions evaluated as half of the load from the preceding beam and half from the subsequent beam. For a constant distributed load $q_0 = \dfrac{\mathbf{h}_t \cdot \mathbf{q}_t}{\Theta}$, the particular solution simplifies to:

$$r_{t,P} = \frac{r_o^4 q_0}{24\, E\, I_o}\, \theta^4, \qquad r_{t,P}^{(1)} = \frac{r_o^4 q_0}{6\, E\, I_o}\, \theta^3. \tag{37}$$

Boundary conditions are applied at the contact points, assuming zero slope at the ball contacts as a first approximation:

$$\begin{cases} r_t(0) = r_{o-1}, \qquad r_t^{(1)}(0) = r_{o-1}^{(1)} = 0, \\ r_t(\Theta) = r_{o+1}, \quad r_t^{(1)}(\Theta) = r_{o+1}^{(1)} = 0, \end{cases} \tag{38}$$

where $r_t^{(1)}$ denotes the angular derivative of the transverse displacement (i.e., the slope).
For convenience, the following auxiliary quantities are introduced:

$$\Delta r_o = r_{o+1} - r_{o-1}, \qquad \Sigma r_o^{(1)} = r_{o+1}^{(1)} + r_{o-1}^{(1)}; \qquad \xi_t = \frac{\theta}{\Theta}. \tag{39}$$

the solution constants become:

$$\begin{aligned} &A_0 = r_{o-1}; \qquad A_1 = r_{o-1}^{(1)} = 0; \\ &A_2 = \frac{3\, \Delta r_o}{\Theta^2} - \frac{r_o^4\, q_0\, \Theta^2}{24\, E\, I_o}; \\ &A_3 = -\frac{2\, \Delta r_o}{\Theta^3} - \frac{r_o^4\, q_0\, \Theta}{12\, E\, I_o}. \end{aligned} \tag{40}$$

Thus, the local radius along the segment is:

$$r_t(\theta) = r_{o-1} + \xi_t^2 \left(3\, \Delta r_o - \frac{r_o^4\, q_0\, \Theta^4}{24\, E\, I_o}\right) + \xi_t^3 \left(-2\, \Delta r_o - \frac{r_o^4\, q_0\, \Theta^4}{12\, E\, I_o}\right). \tag{41}$$

$$r_t(\theta) = r_{o-1} + \left(3\, \xi_t^2 - 2\, \xi_t^3\right) \Delta r_o - \frac{r_o^4\, q_0\, \Theta^4}{12\, E\, I_o} \left(\frac{\xi_t^2}{2} + \xi_t^3\right). \tag{42}$$

This expression provides a smooth, continuous radial displacement field between adjacent contact points, preserving both displacement and slope at the boundaries. If the radii at the ends are equal and the load is null, the sector remains circular.

It should be noted that the reconstruction of the outer-ring deformation through simply supported beam segments represents an approximation of the actual structural behavior of a closed ring. In a continuous ring, the deformation is governed by compatibility of both displacement and internal forces, and the bending moment is generally non-zero at the contact points.

It is important to clarify that the angular coordinate used in the beam reconstruction does not refer to the position of the sphere centers, but to the angular location of the contact points between the rolling elements and the outer ring. By construction, these contact points correspond to locations where the rolling elements are locally tangent to the raceway profile. As a consequence the local deformation of the outer ring exhibits a stationary condition at these points.

Under this interpretation, the assumption of zero slope at the boundaries of each beam segment represents a first-order approximation of the local geometric condition at the contact points, where the deformation curve transitions between adjacent segments. This choice ensures continuity of the reconstructed profile and avoids artificial kinks or discontinuities in the ring geometry. Moreover, since the contact points are defined in terms of the actual interaction geometry rather than the angular position of the sphere centers, the imposed boundary condition remains consistent with the physical configuration of the bearing. While this approximation neglects the exact bending moment distribution at the contact, it provides a geometrically meaningful and numerically stable representation of the ring deformation suitable for the present modeling framework.

The global continuity of the ring is not enforced at the level of individual beam segments, but is ensured through the sector-based dynamic formulation and the homogenization coupling term. As a result, the reconstructed deformation field remains smooth and physically consistent at the global level, despite the local simplification of the boundary conditions.

This modeling choice allows capturing the dominant deformation mechanisms of the ring with a reduced computational cost, which is essential for integration within multibody dynamic simulations. Nevertheless, the assumption introduces a local approximation in the bending moment distribution.

3. Results

After establishing the mathematical model of the bearing, the next step is to analyse the static and dynamic behaviour predicted by the formulation. To this goal, a simulation campaign was performed. The main computational steps of the simulation procedure are summarized below:

- The initial geometry of the bearing is defined, including the undeformed radii, number of rolling elements, and preload conditions.
- The inner ring deformation is imposed through the elliptical kinematics, allowing the positions of the contact points to be determined.
- For each time step, the contact forces between rolling elements and races are computed.
- The dynamic equilibrium of the outer-ring sectors is solved in the normal direction, accounting for contact forces, homogenization forces, anchoring forces, and external loads.
- The deformation of the outer ring between contact points is reconstructed using the beam-based formulation, ensuring continuity of displacement and slope.
- The tangential dynamics of the rolling elements and outer ring are then updated, including frictional interactions and cage effects.
- The procedure is repeated over time to obtain the dynamic evolution of the system.

To assess the predictive capability of the proposed DFM formulation, the model predictions are compared with independent experimental measurements reported in the literature. The comparison focuses on the quantities directly governed by the proposed bearing formulation, namely the angular distribution of rolling-element load, the location and width of the load zone, and the outer-ring radial deformation.

As an illustrative case study, the model has been applied to a representative harmonic drive bearing configuration using the parameters reported in Tables 1 and 2. The results demonstrate the capability of the model to capture the coupled dynamics of rolling elements, deformable races, and nonlinear contact interactions, while maintaining numerical stability and computational efficiency.

3.1. Static behavior

Before analysing the system dynamics, it is essential to characterize the static deformation of the bearing-cam assembly, as this configuration establishes the baseline load distribution and determines the initial conditions for the dynamic simulations. In particular, two quantities are primarily interesting: the compression of the rolling elements and the radial dilation of the outer ring sectors. These variables directly reflect how the elliptical geometry of the inner race, the preload, and the deformability of the outer race combine to shape the static equilibrium of the bearing (Fig. 16). Understanding the static response is therefore crucial, since it governs the load zone extension, the stiffness distribution along the circumference, and the resulting force transmission through the mechanism.

In the static condition, the rolling-element compression exhibits the expected trend imposed by the elliptical shape of the inner race: the maximum compression occurs in correspondence with the major axis, while the minimum is observed along the minor axis. The compression on the minor axis is not zero due to the preload, which ensures continuous contact between spheres and races even in regions of reduced radial interference.

The dilation of the outer ring sectors follows a similar pattern: maximum expansion occurs along the major semi-axis, while the deformation is minimal along the minor one. Although ball compression and sector dilation share the same angular dependence, their

Table 1
Geometric and structural parameters of the simulated bearing.

Parameter	Symbol	Value
Inner ring undeformed radius	r_{i0}	15.69 mm
Inner ring eccentricity	w_0	0.5 mm
Number of spheres	N_b	23
Spheres radius	r_s	1.6 mm
Number of outer ring sectors	N_o	23
Outer ring undeformed radius	r_{o0}	18.89 mm
Rings thickness	s_b	1 mm
Rings height	h_b	5 mm
Number of outer ring beam discretization	N_t	200

Table 2
Mass, inertia, stiffness and friction parameters used in the bearing dynamic model.

Parameter	Symbol	Value
Steel density	ρ_{steel}	7850 kg/m^3
Steel Young's modulus	E_{steel}	206 GPa
Steel Poisson's ratio	ν_{steel}	0.30
Damping coeff.	ζ	1.1
Bearing normal stiffness	k_b	7.1×10^7 $N/m^{3/2}$
Bearing tangential stiffness	k_{bt}	7.1×10^5 N/m
Contact exponent	γ_b	$3/2$
Cage stiffness	k_c	1.7×10^3 N/rad
Homogenization stiffness	k_h	7.1×10^2 N/m
Anchoring stiffness	k_a	5.0×10^4 N/m
Preload factor	k_{pl}	0.95
Static friction coeff.	μ_s	0.30
Coulomb friction coeff.	μ_C	0.20
Stribeck velocity	v_S	0.01 m/s
Smoothing velocity	v_ϵ	10^{-3} m/s
Viscous friction term	k_μ	0.06 s/m
Rolling resistance torque	T_0	10^{-5} Nm
Rolling viscous coeff.	B	10^{-6} $Nm/rad/s$
Characteristic roll speed	ω_s	10^{-2} rad/s

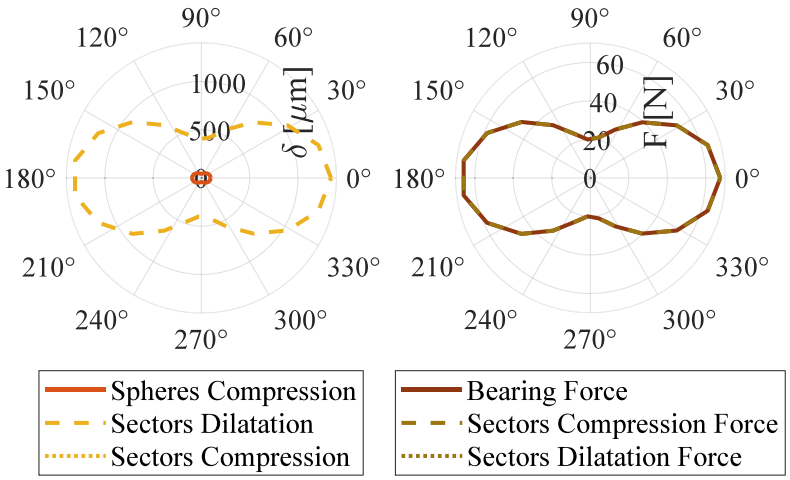

Fig. 16. Comparison between spheres compression and sectors dilatation/compression and between bearing force and sectors compression/dilatation force.

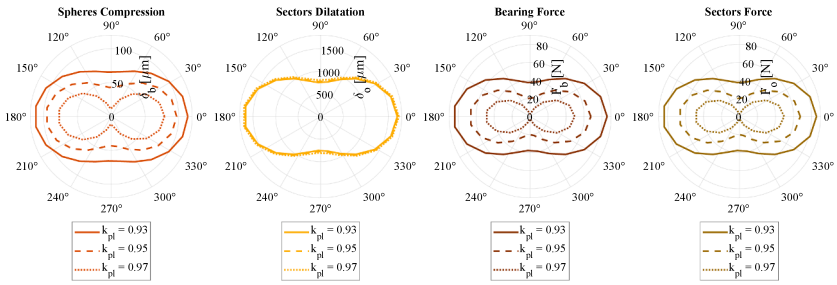

Fig. 17. Sensitivity analysis on spheres compression, sectors dilatation, bearing force and sectors force depending on different level of preload factor.

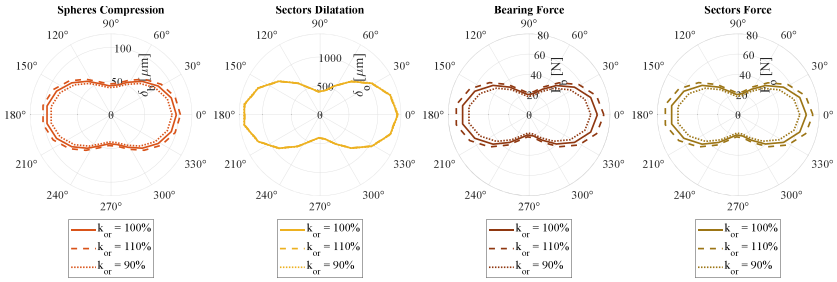

Fig. 18. Sensitivity analysis on spheres compression, sectors dilatation, bearing force and sectors force depending on different level of outer ring stiffness.

force-displacement behaviour differs. This is due not only to the distinct stiffness values of the illustrative springs used in the model, but also to the inherently nonlinear nature of the Hertzian contact law governing the bearing forces.

From a static standpoint, the most relevant quantities are the force transmitted through the rolling elements and the elastic reaction of the outer ring sectors (Fig. 16). For equilibrium to hold, these two forces must balance each other at every angular position. This condition guarantees that the outer ring deformation is compatible with the load distribution imposed by the elliptical inner race and the preload, ensuring a consistent static configuration from which the dynamic behaviour can be meaningfully studied.

A comparison between the force magnitude and distribution predicted by the present model and those reported in [12,31] shows strong consistency. Specifically, the maximum force level is approximately 60N, and the characteristic double-lobe distribution is accurately captured, with peak forces oriented along the major axis and negligible forces along the minor axis.

The force magnitude is governed by several parameters, primarily the stiffness of the components (i.e., material properties) and the preload factor, which ensures sustained contact between the rolling elements and both raceways. In order to evaluate the robustness of the proposed model and to assess the influence of key parameters on the predicted behavior, a sensitivity analysis has been carried out.

The influence of the preload factor has been investigated by considering three representative values (0.93, 0.95, and 0.97). The results are reported in Fig. 17. As shown, the preload primarily affects the overall magnitude of the system response, while preserving the angular distribution of the deformation and forces. In particular, an increase in preload leads to a uniform increase in sphere compression and contact forces along the entire circumference, as well as a corresponding increase in the outer-ring sector forces. This behavior is consistent with the physical role of preload, which introduces a baseline compressive state in the bearing, ensuring continuous contact between rolling elements and races.

The angular position of maximum compression and force remains aligned with the major axis of the elliptical deformation, independently of the preload level. However, the minimum compression region (near the minor axis) is significantly affected by preload variations, with higher preload values reducing the amplitude of load fluctuations and preventing near-zero contact conditions. This confirms that the preload factor plays a crucial role in stabilizing the load distribution and avoiding loss of contact, while having a limited influence on the spatial pattern of deformation.

The influence of the outer ring stiffness has been evaluated by scaling both the homogenization and anchoring stiffness coefficients by ±10% with respect to their nominal values. The results are shown in Fig. 18. Unlike the preload factor, variations in stiffness mainly affect the amplitude of the outer-ring deformation, with stiffer configurations resulting in reduced sector dilation and softer configurations leading to increased deformation. The sphere compression and bearing forces are only moderately influenced by stiffness variations, indicating that the global load distribution is primarily governed by the imposed kinematics of the inner ring and the contact mechanics.

Importantly, the overall shape of the deformation and force distributions remains unchanged across all tested configurations, demonstrating that the proposed model is robust with respect to reasonable variations of the stiffness parameters. This result supports the physical consistency of the formulation and indicates that the model predictions are not overly sensitive to parameter tuning.

3.2. Dynamic behavior

The sequence of plots in Figs. 19 and 20 illustrates the time-evolving deformation of the compliant bearing keyed on the rotating elliptical cam. Each frame reports the instantaneous geometry of the inner ring (IR) and outer ring (OR), together with the positions of the rolling elements and the corresponding contact points. The superposition between the reference undeformed geometry and the current configuration highlights how the structure accommodates the continuously varying load direction imposed by the cam rotation. The inner ring follows the exact elliptical profile, while the outer ring undergoes a non-uniform radial deformation that evolves in time as the load zone migrates along the circumference.

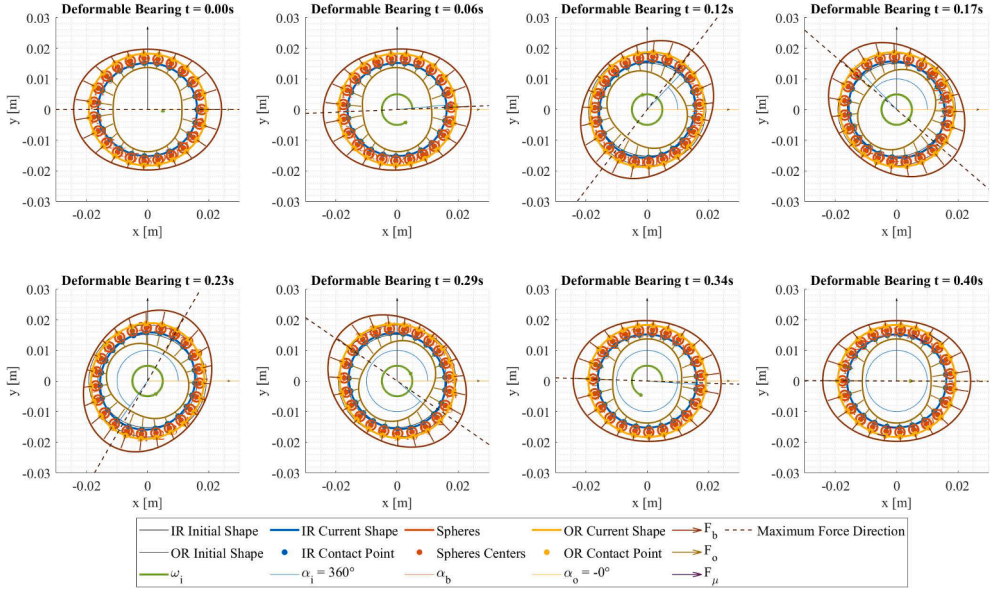

Fig. 19. Representation of the dynamic configurations of the deformable bearing keyed on the rotating elliptical cam.

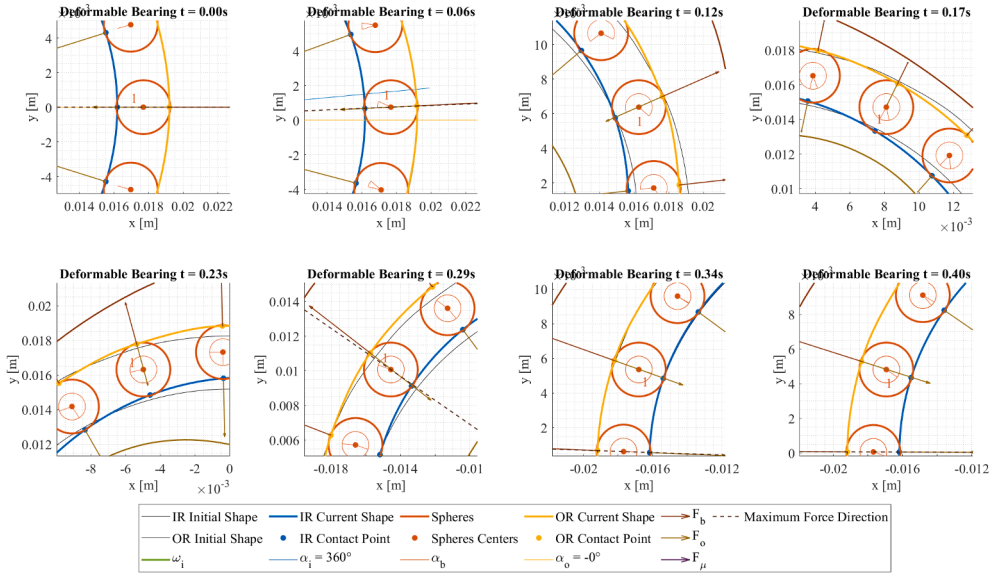

Fig. 20. Representation of the dynamic evolution of the first sphere and associated sector.

As the cam rotates, certain angular sectors periodically expand or contract depending on whether they belong to the instantaneous load zone or to the unloaded region. This behaviour is consistent with the migration of the Hertzian contact patch, which is clearly observable through the changing locations of the force vectors acting on the rolling elements.

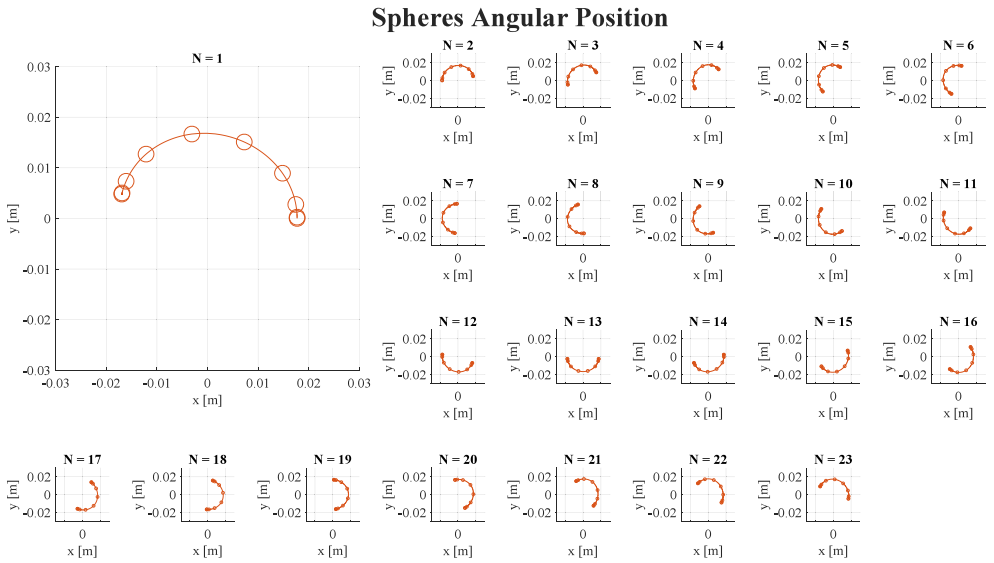

Fig. 21. Revolution motion of the rolling elements around the bearing center.

3.3. Motion, deformations and forces analysis

While the angular position of the inner ring is directly imposed so that a full revolution is completed over the simulation time, the angular trajectories of the spheres arise entirely from the system dynamics. The interaction forces between the spheres and the two races and the kinematic constraints induced by the cage cause each rolling element to follow a trajectory qualitatively similar to that of the inner ring, although with a reduced angular excursion. This behaviour ensures that the mutual angular spacing between the spheres remains nearly constant, apart from small oscillations associated with local vibrations.

A more detailed view of the rolling element revolution is provided in Fig. 21, where the frames, evenly spaced in time, clearly show how the instantaneous angular velocity of each sphere is driven by the imposed rotational speed of the inner ring. As expected, the spheres orbit around the bearing center with a kinematic law that reflects the time-varying deformation of the races and the frictional interactions at the contacts.

Fig. 22 reports instead the spin motion of the individual spheres. All the rolling elements complete approximately five rotations about their own centers over a cycle, in agreement with the expected kinematic relationship between orbital motion and local rolling induced by the inner-outer race velocity mismatch.

Finally, Fig. 23 illustrates the evolution of the linearised system, which can be interpreted as the superposition of four characteristic motions. First, the rotational motion of the inner ring, represented along the horizontal axis, periodically shifts the major and minor semi-axes of the elliptical cam. Second, the spheres exhibit a radial motion (vertical axis) as they follow the deformation imposed by the inner ring geometry. Third, they experience a tangential rotational motion (horizontal axis), associated with their spin generated by frictional interaction with both races. The last component corresponds to the radial deformation of the outer ring sectors, constrained externally against rotation but free to expand and contract according to the local load distribution.

During the rotation of the elliptical cam, the regions of maximum sphere compression and maximum outer-ring dilatation follow the evolution of the major semi-axis, as expected from the imposed geometric constraint.

Fig. 24 shows the time evolution of the deformation of each rolling element (top plot) together with the radial dilation of the corresponding virtual sector of the outer ring (bottom plot). Each curve represents the response of a single sphere or sector during one full revolution of the elliptical cam. In the upper graph, the compression histories form a family of sinusoid-like waves that are mutually phase-shifted. Their amplitude ranges approximately between 0.03 mm and 0.13 mm, revealing the periodic loading and unloading experienced by each rolling element. The curves do not collapse to a common value at any instant, indicating that the load peak is reached at different times depending on the initial angular position of the element. The envelope of all curves confirms that the global load transmitted through the bearing remains essentially unchanged during the cam rotation, but has a peak when the bearing inner ring reaches the maximum rotation speed.

A similar behaviour can be observed in the bottom plot, which reports the deformation of the virtual sectors of the outer ring. Although the waveform closely resembles that of the rolling elements, the amplitude is bigger (typically between 0.9 and 1.8 mm), reflecting the different stiffness of the ring compared to the Hertzian compression of the spheres. The phase shift between curves persists, and the ordering of the deformation peaks mirrors that observed for the spheres: whenever a rolling element reaches its maximum compression, the associated sector undergoes its maximum radial expansion.

The origin of this characteristic deformation pattern lies in the combined effect of the kinematics and load redistribution in a compliant bearing actuated by a rotating elliptical cam. The cam imposes a periodically varying radial displacement on the inner

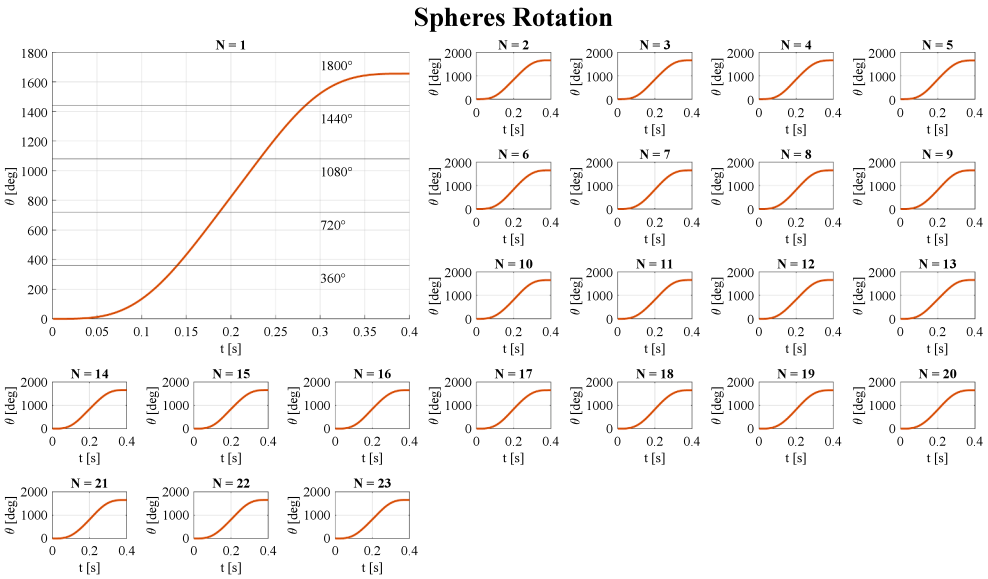

Fig. 22. Spin rotation of each rolling element around its own center.

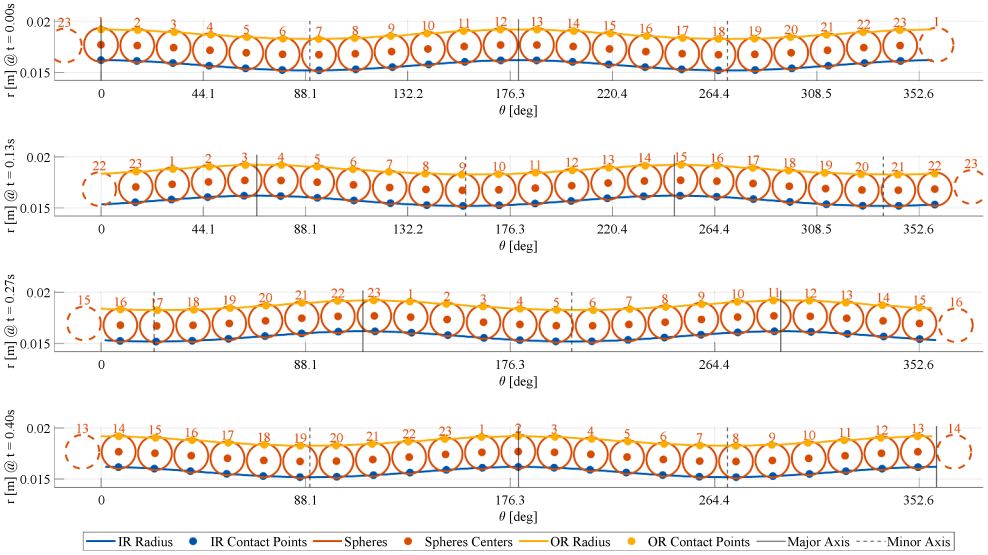

Fig. 23. Time evolution of the linearised model showing the superposition of the principal motion components.

ring, which attains its maximum at the major axis and its minimum at the minor axis. Meanwhile, each sphere travels around the raceway with an angular velocity proportional to the cam rotation, so the instant at which it encounters the major or minor axis depends on its initial angular position. This mechanism introduces the phase differences observed among the deformation curves. In addition, the deformability of the outer ring causes the load zone to migrate along the circumference: each rolling element cyclically enters and exits the load zone, generating alternating phases of high and low compression.

Overall, the resulting “woven” pattern of deformation histories encapsulates the essential features of the system dynamics: the geometric asymmetry of the elliptical cam, the orbital motion of the rolling elements, the elastic anisotropy of the outer ring, and the continuous quasi-static redistribution of forces along the raceway. This interplay between geometry, kinematics, and elasticity explains the distinct phase-shifted, periodic behaviour displayed in the plots.

3.3.1. Influence of the load conditions

In this part of the paper, the effect of an externally applied distributed load is investigated. As previously discussed, the distributed load is modeled through a discrete set of equivalent forces, with one force associated to each tooth of the flexspline, which will be explicitly included in the complete model developed in future work. Clearly, this approximation can be systematically refined by increasing the number of discretization points, denoted by N_t.

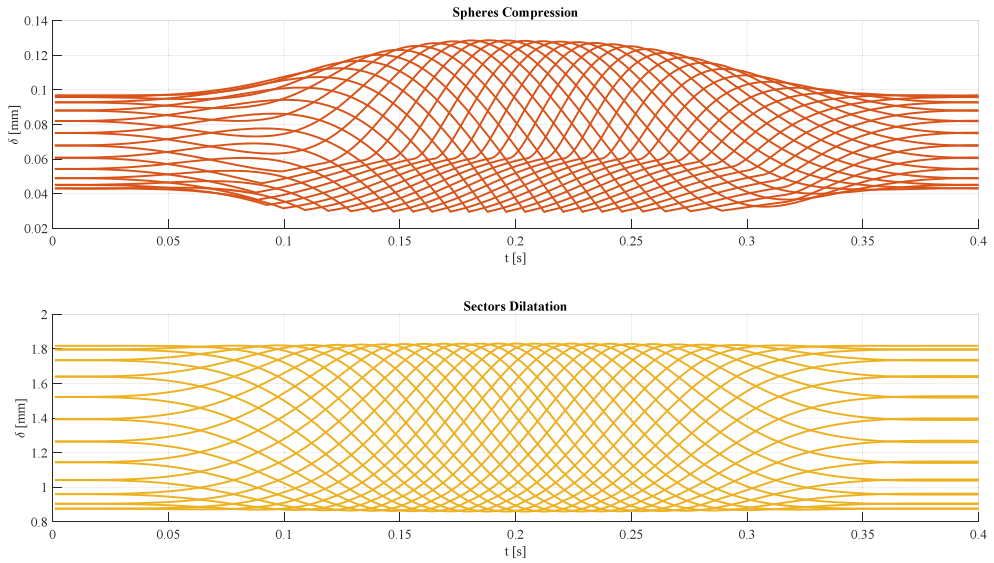

Fig. 24. Time evolution of spheres compression and sectors dilatation.

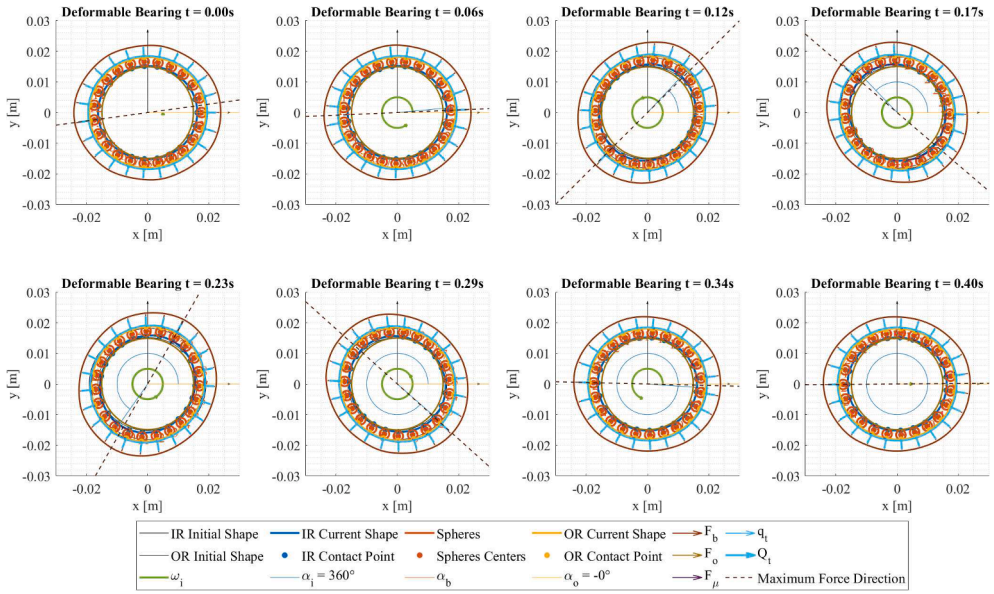

Fig. 25. Representation of the dynamic configurations of the deformable bearing keyed on the rotating elliptical cam with a constant distributed discrete load.

Because the number of teeth interacting with each virtual sector is not uniform, the resulting force shape of both the bearing and the sectors retain the same qualitative structure observed under unloaded conditions, but appear slightly less homogeneous. Moreover, the presence of a constant external load acting on the overall ring leads to a global increase in the forces transmitted through the rolling elements, while the restoring forces developed by the sectors are correspondingly reduced (Fig. 25). This behaviour reflects the redistribution of the load between the bearing contacts and the compliant outer ring induced by the superposition of the distributed excitation.

By analysing the curves reported in Fig. 26, it can be observed that the presence of a load symmetric with respect to the x-axis induces a marked increase in the bearing forces in the region where the external load reaches its maximum, namely along the positive x-axis. This increase is accompanied by a corresponding reduction in the restoring forces developed by the outer-ring sectors. Since the applied load is constant in time, the temporal evolution of the bearing forces is modified so as to accommodate the superposition of the applied load and the forces arising from the deformation imposed by the cam. As a result, the force patterns preserve their periodic nature, while their amplitude and spatial distribution are altered by the presence of the external excitation.

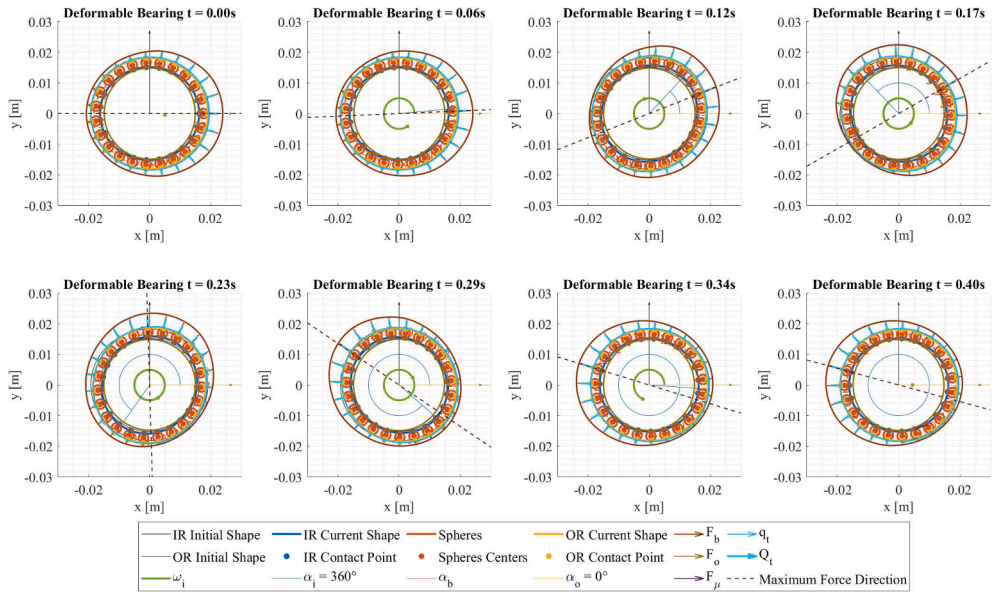

Fig. 26. Representation of the dynamic configurations of the deformable bearing keyed on the rotating elliptical cam with a simmetrical distributed discrete load.

3.4. Validation against independent experimental data and benchmark models

The predictive capability of the proposed DFM formulation was assessed through two complementary validation levels. First, the experimentally observable consequences of the internal load redistribution were compared with published measurements and numerical analyses of elliptically deformed ball bearings in strain-wave gearings [19,51,52]. Second, the internal quantities that cannot be measured directly inside an assembled harmonic drive without intrusive instrumentation, namely the rolling-element load distribution and the load-zone extension, were compared with analytical and FEM-based benchmark models available in the literature [12,29,53].

This validation strategy is adopted because direct measurement of the force transmitted by each individual ball would require an instrumented bearing and would likely modify the compliance distribution that must be validated. Conversely, the same load redistribution mechanism produces experimentally accessible quantities, such as the radial acceleration of the surrounding elastic structure and the characteristic order content of the vibration response. The quantities considered in the validation are therefore

$$F_{b,j}(\theta,t), \qquad u_o(\theta,t), \qquad a_o(\theta_s,t)=\frac{\partial^2 u_o(\theta_s,t)}{\partial t^2}, \tag{43}$$

where $F_{b,j}$ is the contact force transmitted by the jth rolling element, u_o is the radial displacement of the outer ring, a_o is the radial acceleration at the sensor angular position θ_s, and θ is measured in the bearing plane.

For the dynamic comparison, the error was evaluated in the order domain. Let

$$\eta=\frac{f}{f_n} \tag{44}$$

be the order associated with a spectral component, where f_n is the input-shaft rotational frequency. The order and frequency errors are defined as

$$E_\eta=\eta_{\mathrm{DFM}}-\eta_{\mathrm{ref}}, \qquad E_f=f_{\mathrm{DFM}}-f_{\mathrm{ref}}. \tag{45}$$

For the static and quasi-static load-distribution benchmarks, the relative errors in the maximum ball load and in the load-zone extension are defined as

$$E_F=\frac{|F^{\max}_{b,\mathrm{DFM}}-F^{\max}_{b,\mathrm{ref}}|}{F^{\max}_{b,\mathrm{ref}}}100, \qquad E_\phi=\frac{|\phi_{L,\mathrm{DFM}}-\phi_{L,\mathrm{ref}}|}{\phi_{L,\mathrm{ref}}}100, \tag{46}$$

where ϕ_L is the angular extension of the loaded region. The angular position of the maximum load is assessed with respect to the major axis of the elliptic deformation.

3.4.1. Comparison with dynamic data

The works of Skowronek and co-workers are used as an independent dynamic benchmark because they investigate the same physical configuration considered here: a bearing deformed by an elliptic wave generator and coupled to a compliant outer structure.

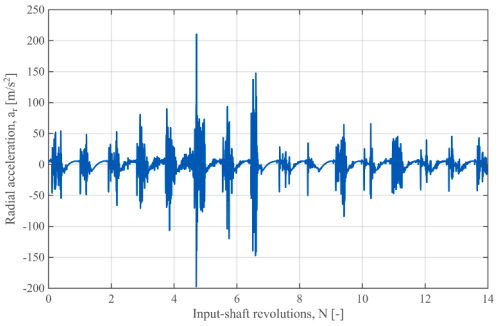

(a) Radial acceleration.

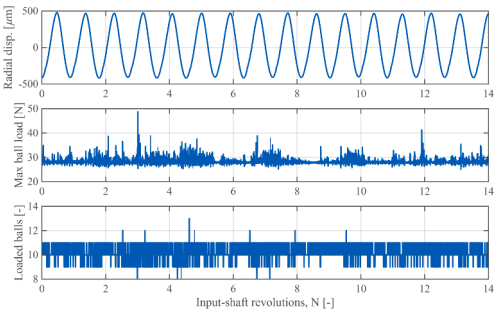

(b) Displacement, maximum ball load, and number of loaded balls.

Fig. 27. DFM time-domain response for the *SkDAGA* case at 1000 rpm.

In the DAGA test stand, the bearing is strained between an elliptic disk and an elastic pan; the disk rotates at 1000 rpm and the radial acceleration is measured on the elastic pan [52]. The same study reports that even an undamaged elliptically deformed bearing generates impulse-shaped acceleration signals, and that the corresponding characteristic components are more clearly identified in the envelope spectrum than in the standard amplitude spectrum. The work in [19] further showed that negative impulses arise when balls pass the angular positions of maximum contact force, while positive impulses are associated with contact loss and re-contact due to radial tolerance.

The geometry adopted in the DFM simulations follows the reference data reported by Skowronek:

$$D_B = 4.75\,\text{mm}, \qquad D_P = 42.31\,\text{mm}, \qquad N_b = 23, \tag{47}$$

where D_B is the ball diameter, D_P is the pitch diameter, and N_b is the number of balls. The angular spacing between adjacent balls is

$$\Delta\theta_b = \frac{360^\circ}{N_b} = 15.65^\circ. \tag{48}$$

The characteristic bearing frequencies are computed using the same expressions adopted in the reference works:

$$\begin{aligned} f_c &= \frac{1}{2} f_n \left(1 - \frac{D_B}{D_P}\right), \\ f_I &= \frac{1}{2} f_n N_b \left(1 + \frac{D_B}{D_P}\right), \\ f_O &= \frac{1}{2} f_n N_b \left(1 - \frac{D_B}{D_P}\right), \\ f_B &= f_n \left(\frac{D_P}{D_B} - \frac{D_B}{D_P}\right). \end{aligned} \tag{49}$$

With the adopted geometry, the corresponding orders are

$$\frac{f_c}{f_n} = 0.4439, \qquad \frac{f_O}{f_n} = 10.2089, \qquad \frac{f_I}{f_n} = 12.7911, \qquad \frac{f_B}{f_n} = 8.7951. \tag{50}$$

The outer-race rollover frequency f_O is also denoted as f_A, because it corresponds to the impulse sequence generated when rolling elements pass through the regions of maximum contact force.

Two operating conditions were simulated. The first one, denoted as *SkNumerical*, corresponds to the numerical condition at 2000 rpm, i.e. $f_n = 33.333$ Hz. The second one, denoted as *SkDAGA*, reproduces the experimental DAGA speed at 1000 rpm, i.e. $f_n = 16.667$ Hz. The same bearing geometry and contact formulation were used in both cases.

Figs. 27 and 28 show that the radial displacement is governed by the periodic motion imposed by the rotating ellipse, whereas the acceleration contains localized impulse-like events. This agrees with the mechanism described in the reference studies: the vibration response is produced by the passage of rolling elements through the high-load regions and by contact changes associated with bearing tolerance.

The DFM model predicts a mean number of loaded balls equal to 10.10 for *SkDAGA* and 9.81 for *SkNumerical*. Since the load pattern is organized into two high-load regions, these values correspond to approximately five balls per loaded sector. This is consistent with the reference load-zone extension of about 80° per ellipse side reported in [52]. Using the ball spacing of 15.65°, five balls correspond to

$$5\Delta\theta_b = 5\frac{360^\circ}{23} = 78.3^\circ. \tag{51}$$

It should be noted that the reference studies also indicate that most of the deformation is carried by the central two or three balls within each loaded sector. Therefore, the DFM result should be interpreted as agreement in the overall load-zone extension rather than as an exact match of the detailed force sharing within each sector.

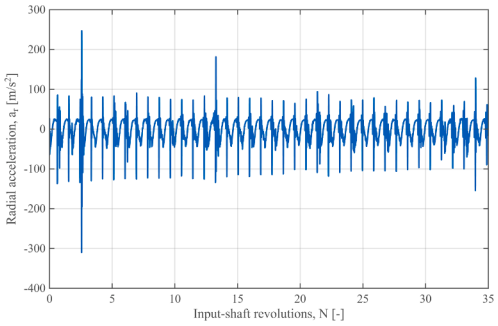

(a) Radial acceleration.

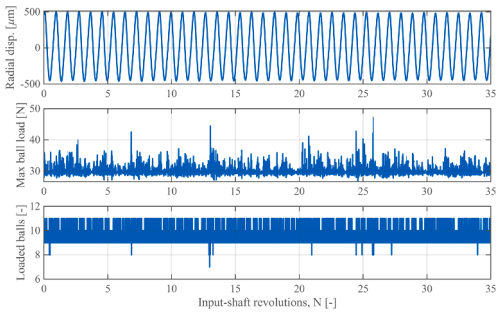

(b) Displacement, maximum ball load, and number ofloaded balls.

Fig. 28. DFM time-domain response for the *SkNumerical* case at 2000 rpm.

Table 3
Comparison of the DFM load-zone extension with the load-zone interpretation of Skowronek.

Quantity	Reference data	DFM prediction	Error
Load-zone extension per sector	about 80°	78.3°	−2.1%
Mean loaded balls, 2000 rpm	∼10	∼10	–
Mean loaded balls, 1000 rpm	∼10	∼10	–
Main force concentration	central balls of each sector	central balls of each sector	qualitatively matched

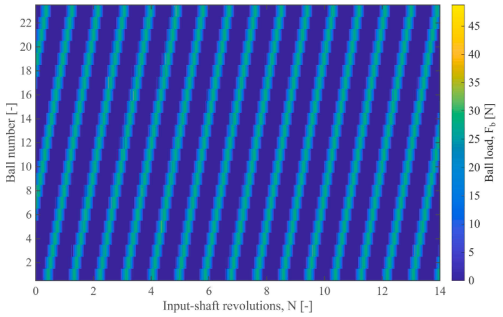

(a) *SkDAGA*.

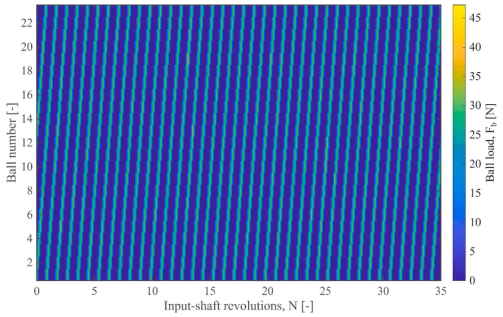

(b) *SkNumerical*.

Fig. 29. Ball-load maps predicted by the DFM model. The diagonal bands show the periodic passage of the rolling elements through the two loaded sectors generated by the rotating elliptic deformation.

The ball-load maps in Fig. 29 confirm that the loaded sectors migrate periodically with the rotating ellipse. The instantaneous distributions in Fig. 30 show two separated loaded regions and negligible load over a substantial part of the circumference. The maximum ball loads are 47.23 N for *SkNumerical* and 48.73 N for *SkDAGA*; the corresponding maximum sums of ball forces are 227.45 N and 209.48 N, respectively (Table 3).

Figs. 31 and 32 show the order-domain spectra obtained from the simulated acceleration. The dashed vertical lines denote the theoretical characteristic orders. In both operating conditions, local spectral maxima are found close to the expected components. Low-order components, especially around the first and second orders, remain prominent because the sensor displacement is strongly influenced by the imposed elliptic deformation and by the reduced-order support representation. For this reason, the validation is based on the position of the characteristic order components rather than on their absolute dominance in the spectrum. The envelope spectra are used as an additional indicator because the reference experimental study identifies impulsive phenomena more effectively through envelope analysis.

The maximum order error in the selected components is below 0.15 orders. This corresponds to less than 5 Hz at 2000 rpm and less than 2.5 Hz at 1000 rpm. The result confirms that the DFM model reproduces the characteristic order structure of the elliptically deformed bearing: the rotating ellipse produces the low-order periodic deformation, the rolling elements periodically cross the two loaded sectors, and the resulting impulse-like acceleration contains local spectral peaks at the expected bearing orders (Tables 4–5).

3.4.2. Comparison with analytical and FEM-based load-distribution benchmarks

The second validation level concerns internal quantities that are not directly measured in the Skowronek test bench, but are available from established analytical and FEM-based studies on flexible bearings in harmonic reducers. In particular, the DFM load distribution was compared with the results reported by Li et al. [12] and Yu et al. [29]. These comparisons assess whether the model

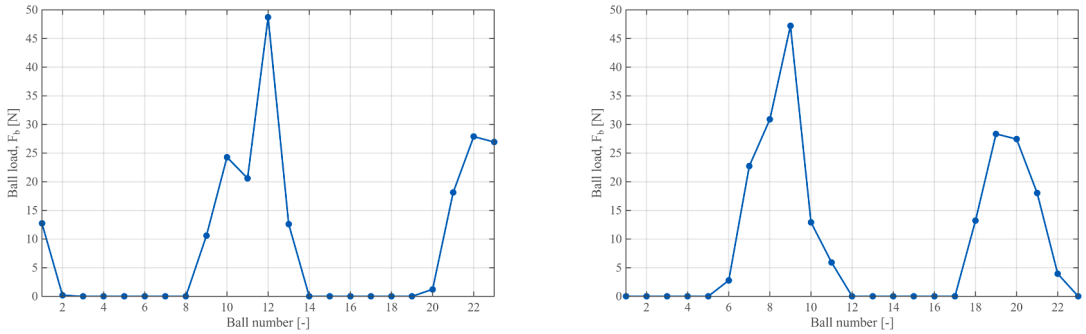

(a) *SkDAGA*. (b) *SkNumerical*.

Fig. 30. Instantaneous ball-load distributions at the global maximum force. The two localized loaded regions are consistent with the load-transfer mechanism reported for elliptically deformed bearings.

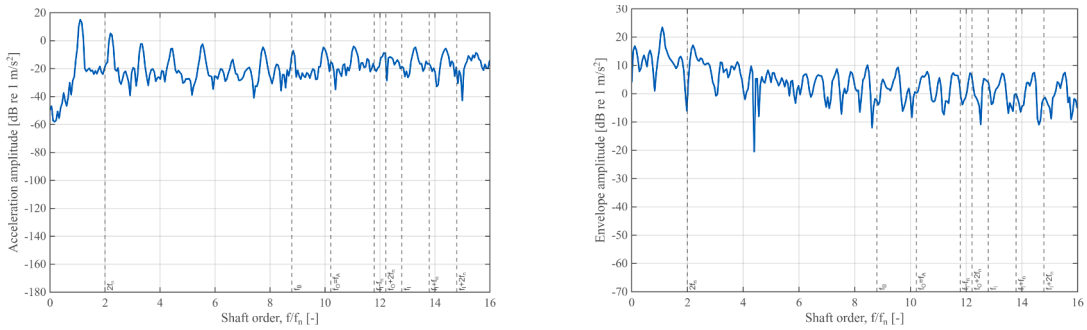

(a) Acceleration spectrum. (b) Envelope spectrum.

Fig. 31. Order-domain spectra of the DFM response for the *SkDAGA* case at 1000 rpm.

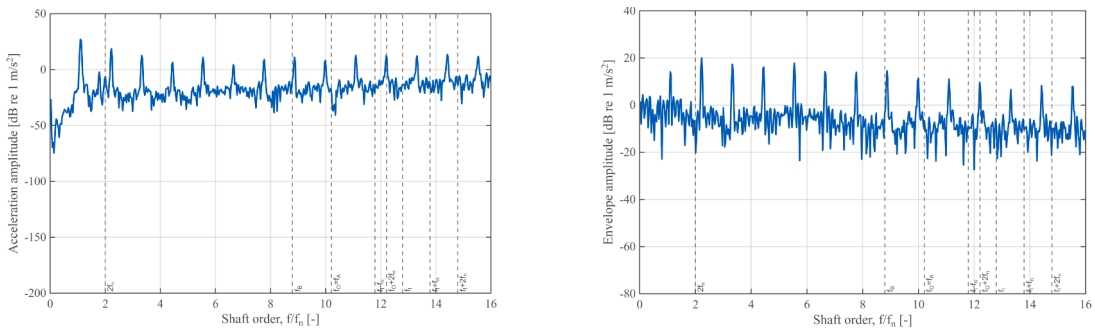

(a) Acceleration spectrum. (b) Envelope spectrum.

Fig. 32. Order-domain spectra of the DFM response for the *SkNumerical* case at 2000 rpm.

Table 4
Order-domain comparison for the *SkNumerical* simulation at 2000 rpm.

Quantity	Reference data	DFM prediction	Error
$2f_n$, acceleration spectrum	2.000, 66.67 Hz	2.005, 66.83 Hz	+0.005, +0.17 Hz
$f_O = f_A$, envelope spectrum	10.2089, 340.30 Hz	10.135, 337.83 Hz	−0.074, −2.47 Hz
f_B, envelope spectrum	8.7951, 293.17 Hz	8.8715, 295.72 Hz	+0.076, +2.55 Hz
$f_I - f_n$, envelope spectrum	11.7911, 393.04 Hz	11.920, 397.34 Hz	+0.129, +4.30 Hz
f_I, envelope spectrum	12.7911, 426.37 Hz	12.772, 425.72 Hz	−0.019, −0.65 Hz
$f_I + f_n$, envelope spectrum	13.7911, 459.70 Hz	13.760, 458.68 Hz	−0.031, −1.02 Hz
$f_I + 2f_n$, envelope spectrum	14.7911, 493.04 Hz	14.722, 490.72 Hz	−0.069, −2.31 Hz
$f_O + 2f_n$, acceleration spectrum	12.2089, 406.96 Hz	12.195, 406.49 Hz	−0.014, −0.47 Hz

Table 5
Order-domain comparison for the *SkDAGA* simulation at 1000 rpm.

Quantity	Reference data	DFM prediction	Error
$2f_n$, acceleration spectrum	2.000, 33.33 Hz	2.142, 35.71 Hz	+0.142, +2.37 Hz
f_c, envelope spectrum	0.4439, 7.40 Hz	0.4395, 7.32 Hz	−0.004, −0.07 Hz
$f_O = f_A$, envelope spectrum	10.2089, 170.15 Hz	10.327, 172.12 Hz	+0.118, +1.97 Hz
f_B, envelope spectrum	8.7951, 146.59 Hz	8.734, 145.57 Hz	−0.061, −1.02 Hz
$f_I - f_n$, envelope spectrum	11.7911, 196.52 Hz	11.646, 194.09 Hz	−0.146, −2.43 Hz
f_I, envelope spectrum	12.7911, 213.18 Hz	12.689, 211.49 Hz	−0.102, −1.70 Hz
$f_I + f_n$, envelope spectrum	13.7911, 229.85 Hz	13.788, 229.80 Hz	−0.003, −0.05 Hz
$f_I + 2f_n$, envelope spectrum	14.7911, 246.52 Hz	14.832, 247.19 Hz	+0.040, +0.67 Hz
$f_O + 2f_n$, envelope spectrum	12.2089, 203.48 Hz	12.140, 202.33 Hz	−0.069, −1.15 Hz

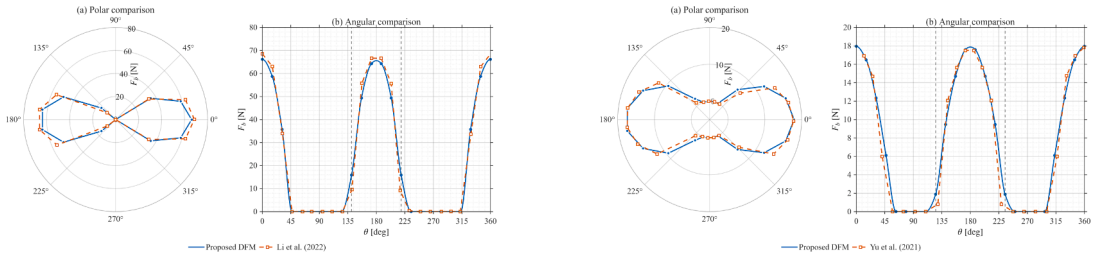

(a) Comparison with Li et al. [12].

(b) Comparison with Yu et al. [29].

Fig. 33. Rolling-element load distribution predicted by the DFM model compared with published load-distribution benchmarks for flexible bearings mounted on elliptical cams.

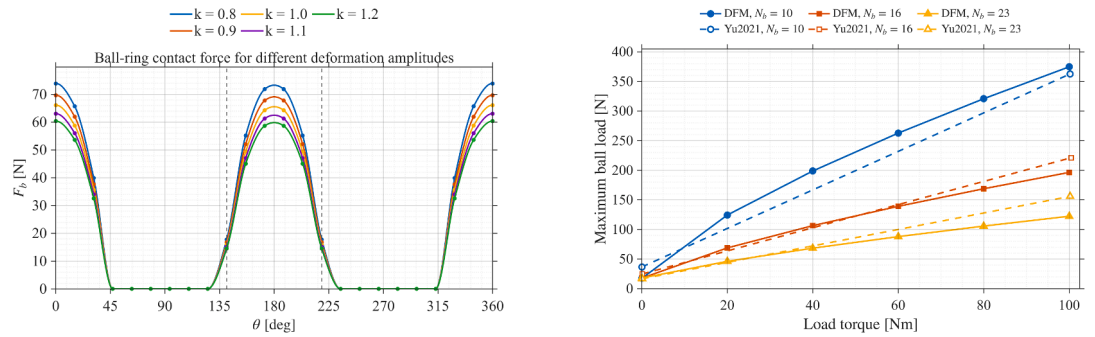

(a) Load of the first ball for different elliptical deformation coefficients.

(b) Maximum ball load as a function of torque and number of balls.

Fig. 34. Additional parametric comparisons with published analytical benchmark trends.

Table 6
Comparison between DFM predictions and the load-distribution benchmark of Li et al. [12].

Quantity	Reference data	DFM prediction	Error
Maximum ball load	66.12 N	63.97 N	3.25%
Angular position of maximum load	major axis	major axis	matched
Load-zone extension	84.59°	86.34°	2.07%
Number of loaded rolling elements	11–12	11–12	matched
Angular position of maximum outer-ring deformation	major axis	major axis	matched

reproduces the characteristic two-lobed ball-load distribution, the location of the load maxima, the number of loaded rolling elements, and the load-zone extension (Tables 6–7).

Fig. 33 shows that the DFM model reproduces the expected two-lobed load distribution, with load maxima in the major-axis regions and reduced or null load near the minor axis. This is consistent with the established interpretation of flexible-bearing behaviour in harmonic reducers: the elliptical wave generator concentrates contact loads near the major axis and unloads the rolling elements close to the minor axis.

The static benchmark comparisons confirm that the DFM formulation captures the internal load redistribution with good accuracy. In the Li et al. benchmark, the maximum ball-load error is 3.25% and the load-zone extension error is 2.07%. In the Yu et al. benchmark, the maximum ball-load error is 0.79%, while the load-zone extension differs by 8.64%. In both cases, the model predicts the correct

Table 7
Comparison between DFM predictions and the load-distribution benchmark of Yu et al. [29].

Quantity	Reference data	DFM prediction	Error
Maximum ball load	17.82 N	17.96 N	0.79%
Angular position of maximum load	major axis	major axis	matched
Load-zone extension	100.39°	109.06°	8.64%
Number of loaded rolling elements	14–15	14–15	matched
Angular position of maximum outer-ring deformation	major axis	major axis	matched

location of the load maxima and the correct number of loaded rolling elements (Fig. 34). Taken together, the dynamic and static comparisons address complementary aspects of the model validation. The dynamic comparison verifies that the DFM model reproduces the experimentally observable vibration mechanism and the characteristic order content of elliptically deformed bearings. The static comparisons verify the internal rolling-element load distribution, which cannot be measured directly in the experimental test bench without intrusive instrumentation. The remaining discrepancies are mainly related to absolute acceleration amplitudes and detailed structural transfer effects, which depend on the elastic pan, sensor dynamics, support compliance, damping, and tribological effects that are represented here through reduced-order equivalent parameters. Therefore, the validation supports the use of the proposed DFM formulation as a computationally efficient model for predicting the dominant load redistribution and vibration mechanisms of deformable ball bearings in harmonic-drive applications.

4. Conclusion

This paper has presented a novel discrete flexible multibody (DFM) model for deformable bearings with flexible rings, specifically, but not only, conceived for harmonic drive applications in which bearing elasticity plays an active functional role. Unlike classical rigid-body or quasi-static bearing formulations, and without the computational burden associated with FEM analyses, the proposed approach provides a physically consistent and computationally efficient framework for capturing the coupled dynamics of rolling elements, deformable races, and nonlinear contact interactions.

The bearing is modeled as an assembly of interacting bodies, where the inner ring, rolling elements, and a discretized outer ring are connected through Hertzian contact laws, friction and rolling-resistance models, and spring-damper elements. The deformation of the outer ring is reconstructed dynamically by representing each circumferential sector as a simply supported Euler-Bernoulli beam, enabling the description of ovalization, sector coupling, preload effects, and load redistribution along the circumference. This homogenized beam-based formulation preserves the global continuity of the ring while remaining compatible with multibody dynamic simulations.

Static analyses demonstrate that the model correctly reproduces the non-uniform load distribution induced by the elliptical deformation of the inner race, including the expected concentration of contact forces along the major semi-axis and the persistence of contact in unloaded regions due to preload. Dynamic simulations further show that the proposed formulation captures the migration of the load zone, the time-varying deformation of the outer ring, and the coupled orbital and spin motion of the rolling elements in a consistent and numerically stable manner. The resulting deformation and force patterns are coherent with the physical operating principles of harmonic drive bearings and confirm the capability of the model to represent deformation-induced interactions over time.

From a comparative standpoint, the proposed DFM formulation provides a balanced trade-off between modeling fidelity and computational cost. In contrast to classical rigid or lumped-parameter bearing models, the present approach explicitly captures ring deformability, nonlinear contact interactions, and circumferential load redistribution. At the same time, compared to high-fidelity finite element models, it significantly reduces computational complexity by avoiding the need for full structural discretization while retaining the essential deformation mechanisms governing the system response. The consistency of the predicted deformation patterns and load distributions with trends reported in FEM-based studies available in the literature further supports the physical soundness of the formulation. These characteristics make the proposed model particularly suitable for system-level simulations of harmonic drive mechanisms, parametric analyses, and design-oriented studies where both accuracy and computational efficiency are required.

Future work will focus on extending the model to include several phenomena like thermo-mechanical effects, wear and lubrication evolution, and more detailed representations of cage dynamics and manufacturing tolerances. In addition, the proposed framework lends itself naturally to Prognostics and Health Management (PHM) applications, as it provides direct access to physically meaningful internal variables such as contact forces, local deformations, slip velocities, and dissipated energy. These quantities can be exploited to define physics-based damage indicators, to simulate the progressive degradation of bearing components, and to support the development of digital twins for condition monitoring and remaining useful life estimation. The comparison with independent experimental data confirms that the proposed formulation reproduces the main experimentally observed features of flexible-bearing behaviour, including the double-lobe load distribution, the location of the maximum contact forces along the major axis, and the reduction of load near the minor axis. Dedicated test-bench experiments remain a future step to further validate high-speed dynamic and tribological effects.

CRediT authorship contribution statement

Roberto Guida: Writing – original draft, Visualization, Validation, Software, Resources, Methodology, Investigation, Formal analysis, Data curation, Conceptualization; **Andrea De Martin:** Writing – review & editing, Supervision, Project administration, Funding acquisition, Conceptualization.

Declaration of competing interest

The authors declare that they have no known competing financial interests or personal relationships that could have appeared to influence the work reported in this paper.

Data availability

No data was used for the research described in the article.

References

[1] B.J. Hamrock, W.J. Anderson, Rolling-Element Bearings, Technical Report, 1983.
[2] H. Cao, L. Niu, S. Xi, X. Chen, Mechanical model development of rolling bearing-rotor systems: a review, Mech. Syst. Signal Process. 102 (2018) 37–58.
[3] C.W. Kennedy, J.P. Desai, Modeling and control of the Mitsubishi PA-10 robot arm harmonic drive system, IEEE/ASME Trans. Mechatron. 10 (3) (2005) 263–274.
[4] K. Ueura, R. Slatter, Development of the harmonic drive gear for space applications, in: 8th European Space Mechanisms and Tribology Symposium, vol. 438, 1999, p. 259.
[5] H.D. Taghirad, P.R. Be' langer, Modeling and parameter identification of harmonic drive systems (1998) 439–444. https://doi.org/10.1115/1.2801484
[6] S.-W. Hong, V.-C. Tong, Rolling-element bearing modeling: a review, Int. J. Precis. Eng. Manuf. 17 (2016) 1729–1749.
[7] H. Dong, K.-L. Ting, D. Wang, Kinematic fundamentals of planar harmonic drives (2011) 011007. https://doi.org/10.1115/1.4003140
[8] S. Lacroix, D. Nélias, A. Leblanc, Four-point contact ball bearing model with deformable rings, J. Tribol. 135 (3) (2013) 031402.
[9] B. You, J. Wen, Load distribution calculation of flexible ball bearing with elliptical cam wave generator, in: International Conference on Mechanics, Materials and Structural Engineering (ICMMSE 2016), Atlantis Press, 2016, pp. 49–55.
[10] H. Jia, H. Xin, Study on lubrication characteristics of novel forced wave generator of harmonic drive without flexible bearing, Materials 15 (1) (2021) 215.
[11] L. Hu, B. Li, Z. Wang, Y. Wang, Analysis and evaluation of multi-state wear mechanism of elastic-flexible thin-walled bearings, Tribol. Int. 202 (2025) 110293.
[12] X. Li, C. Song, C. Zhu, H. Song, Load analysis of thin-walled flexible bearing in harmonic reducer considering assembly with flexspline and cam, Mech. Mach. Theory 180 (2022) 105154.
[13] R. Guida, A.C. Bertolino, A. De Martin, M. Sorli, Comprehensive analysis of major fault-to-failure mechanisms in harmonic drives, Machines 12 (11) (2024) 776.
[14] N. Zheng, J. Wang, M. Wu, H. Liu, Y. Tao, Analysis of flexible bearing load under various torque conditions, Machines 13 (7) (2025) 627.
[15] Y. Xiong, B. Fang, J. Zhang, K. Yan, Y. Zhu, Subsurface stresses analysis of flexible ball bearing with bendable races in a harmonic reducer by superimposition method, Proc. Inst. Mech. Eng. J J. Eng. Tribol. 236 (6) (2022) 1244–1259.
[16] A.C. Bertolino, A. De Martin, G. Jacazio, M. Sorli, Design and preliminary performance assessment of a phm system for electromechanical flight control actuators, Aerospace 10 (4) (2023) 335.
[17] R.H. Lapp, Harmonic drive, 1965. US Patent 3,214,999.
[18] T.D. Tuttle, Understanding and Modeling the Behavior of a Harmonic Drive Gear Transmission, Ph.D. thesis, Massachusetts Institute of Technology, 1992.
[19] C. Adams, A. Skowronek, J. Bös, T. Melz, Vibrations of elliptically shaped bearings in strain wave gearings, J. Vib. Acoust. 138 (2) (2016) 021004.
[20] S. Sumith, A. Gupta, Design and parametric study of flexible ball bearings: a finite element approach, Mater. Today Proc. 56 (2022) 257–262.
[21] H. Cao, Y. Li, X. Chen, A new dynamic model of ball-bearing rotor systems based on rigid body element, J. Manuf. Sci. Eng. 138 (7) (2016) 071007.
[22] R. Gismeros Moreno, F. Marques, E. Corral Abad, J. Meneses Alonso, P. Flores, C. Castejon, Enhanced modelling of planar radial-loaded deep groove ball bearings with smooth-contact formulation, Multibody Syst. Dyn. 60 (1) (2024) 121–159.
[23] X. Hernot, M. Sartor, J. Guillot, Calculation of the stiffness matrix of angular contact ball bearings by using the analytical approach, J. Mech. Des. 122 (1) (2000) 83–90.
[24] R. Pandiyarajan, M.S. Starvin, K.C. Ganesh, Contact stress distribution of large diameter ball bearing using Hertzian elliptical contact theory, Procedia Eng. 38 (2012) 264–269.
[25] J.C. Skurka, Elastohydrodynamic lubrication of roller bearings (1970) 281–288. https://doi.org/10.1115/1.3451388
[26] L. Tian, Y. Jiang, Y. Wang, Q. Tong, D. Su, L. Song, Load distribution research on flexible bearing in harmonic drive, in: International Conference on Mechanical Design, Springer, 2017, pp. 165–176.
[27] V.V. Ivannikov, S.A. Degtyarev, V.V. Popov, F.D. Sorokin, M.K. Leont'ev, Numerical determination of contact forces in radial roller bearings with flexible rings, Russ. Aeronaut. 61 (4) (2018) 567–578.
[28] Z. Caizhi, W. Xiaojing, L. Zhaolun, L. Jun, Z. Jiaqi, Research on static and dynamics mechanical characteristics of flexible bearing in harmonic reducer, Int. J. Adv. Rob. Syst. 17 (2) (2020) 1729881420919953.
[29] Y. Yu, E. Zhu, X. Chen, Y. Wang, Load analysis and deformation research of the flexible bearing based on a three-force ring superposition method, Mech. Ind. 22 (2021) 34.
[30] Z. Zhao, S. Sun, W. Xu, C. Shen, D. Wang, Dynamics modeling and fault diagnosis of flexible thin-walled elliptical bearings in harmonic reducers, Measurement 238 (2024) 115378.
[31] B. Wang, Q. Liu, B. Pang, J. Xu, et al., Dynamic modeling of flexible thin-walled ellipse bearing outer ring fault considering cam disturbance, Nonlinear Dyn. 113 (23) (2025) 32237–32263.
[32] R. Guida, A.C. Bertolino, A. De Martin, M. Sorli, A new computationally efficient model of the non-linear dynamics in harmonic drive reducers, Mech. Mach. Theory 209 (2025) 105992.
[33] A.A. Shabana, Flexible multibody dynamics: review of past and recent developments, Multibody Syst. Dyn. 1 (2) (1997) 189–222.
[34] M. Krack, Systems with contact nonlinearities, in: Model Order Reduction for Design, Analysis and Control of Nonlinear Vibratory Systems, Springer, 2024, pp. 237–275.
[35] P. Guay, A. Frikha, Ball bearing stiffness. A new approach offering analytical expressions, in: Proceedings of 16th European Space Mechanisms and Tribology Symposium, Bilbao, 2015, pp. 23–25.
[36] S.P. Timoshenko, J.M. Gere, Theory of Elastic Stability, Courier Corporation, 2012.
[37] C. Shun, N.J. Hoff, Bending of thin circular rings, Int. J. Solids Struct. 11 (2) (1975) 139–152.
[38] A.C. Bertolino, S. Mauro, G. Jacazio, M. Sorli, Multibody dynamic model of a double nut preloaded ball screw mechanism with lubrication, in: ASME International Mechanical Engineering Congress and Exposition, vol. 84553, American Society of Mechanical Engineers, 2020, p. V07BT07A023.
[39] M.M. Khonsari, E.R. Booser, G. Nikas, On the stribeck curve, Recent Dev. Wear Prev. Frict. Lubr. 661 (2010) 263–278.
[40] M.M. Khonsari, S. Ghatrehsamani, S. Akbarzadeh, On the running-in nature of metallic tribo-components: a review, Wear 474 (2021) 203871.

[41] J. Echávarri Otero, E. de la Guerra Ochoa, E. Chacón Tanarro, F. Franco Martínez, R.W. Contreras Urgiles, An analytical approach for predicting EHL friction: usefulness and limitations, Lubricants 10 (7) (2022) 141.
[42] K.J. Aström, C. Canudas-De-Wit, Revisiting the LuGre friction model, IEEE Control Syst. 28 (6) (2008) 101–114.
[43] V. Van Geffen, A study of friction models and friction compensation, DCT 118 (2009) 24.
[44] F. Al-Bender, Fundamentals of friction modeling, in: Proceedings, ASPE Spring Topical Meeting on Control of Precision Systems, MIT, April 11–13, 2010, vol. 48, ASPE-The American Society of precision Engineering; 301 Glenwood Avenue …, 2010, pp. 117–122.
[45] D.E. Hall, J.C. Moreland, Fundamentals of rolling resistance, Rubber Chem. Technol. 74 (3) (2001) 525–539.
[46] T. Gillespie, Fundamentals of Vehicle Dynamics, SAE international, 2021.
[47] J.A. Greenwood, H. Minshall, D. Tabor, Hysteresis losses in rolling and sliding friction, Proc. R. Soc. London Ser. A. Math. Phys. Sci. 259 (1299) (1961) 480–507.
[48] K.L. Johnson, Contact Mechanics, Cambridge University Press, 1987.
[49] V.L. Popov, et al., Contact Mechanics and Friction, Springer, 2010.
[50] A. Öchsner, Euler–Bernoulli beam theory, in: Classical Beam Theories of Structural Mechanics, Springer, 2021, pp. 7–66.
[51] A.A. Skowronek, Schwingungserregung Durch Elliptisch Verformte Kugellager, Ph.D. thesis, 2013.
[52] A. Skowronek, K. Moritz, J. Bös, T. Melz, Calculated and measured effects of bearing faults in elliptically deformed ball bearings (2014).
[53] Y. Xiong, Y. Zhu, K. Yan, Load analysis of flexible ball bearing in a harmonic reducer, J. Mech. Des. 142 (2) (2020) 022302.